CHALMERS
UNIVERSITY OF TECHNOLOGY

Development of an *in vitro* biological effect assay to assess delivery and efficacy of targeted siRNA to the lung

Master's thesis in Biotechnology

Saied Mohammad Ali Mudarres Sedraee

DEPARTMENT OF LIFE SCIENCES
CHALMERS UNIVERSITY OF TECHNOLOGY

Gothenburg, Sweden 2025
www.chalmers.se

Table of Contents

Acknowledgment

First and foremost, I would like to express my sincere gratitude and appreciation to my supervisor and mentor, Thomas Naessens. Thank you for giving me this golden opportunity to conduct my thesis project at AstraZeneca. I could not have undertaken this journey if it was not for your guidance, expertise and mentorship. I am deeply thankful for the invaluable feedback and support provided by my mangers, Thomas Volckaert and Annika Borde. I am also deeply grateful to my examiner Marcus Wilhelmsson, for providing constructive feedback on this thesis.

Special thanks to Chandra Budida, Rebecka Svärd, Melker Göransson, Martina Klevstig, Beatrice d'Aubigné, Francesca Grasso, Gaberiella Leung and Elin Benatti for training me in the essential skills needed to complete my thesis. I also like to thank everyone in Early Respiratory and Immunology in Gothenburg for their support and making me feel right at home during my stay. It has been a great honour.

Finally, I like to extend my heartfelt thanks to my parents, partner and my friends for their unconditional support and encouragement throughout this wonderful journey.

Abstract

The emergence of small interfering RNA (siRNA) oligonucleotide therapeutics has significantly expanded the druggable target space and has the potential to treat a wide range of diseases with current unmet needs such as idiopathic pulmonary fibrosis (IPF). However, efficacy of siRNA treatments has remained somewhat limited due to issues regarding efficient delivery to target tissues and cells which highlights a major translational barrier. Here, this limitation was addressed by using siRNA conjugated to a small molecule (SM) ligand that is recognized by the epithelial-restricted transmembrane receptor αVβ6-integrin, to specifically deliver siRNA into lung epithelial cells. As part of the proof-of-concept, our goal was to ultimately design an in vitro biological effect assay to evaluate the efficacy of an αVβ6-ligand conjugated siRNA targeting MMP7, a gene product that is believed to play an important role in fibrosis development. To achieve this goal, the assay was developed using 16HBE, A549 and iPSC-derived organoids. The data revealed that, while inflammatory and aberrant basaloid markers were clearly induced in 16HBE and A549 when stimulated with proinflammatory and profibrotic mediators respectively, the cell models did not display the expected MMP7 overexpression pattern. In addition, we demonstrated increased knockdown potency of the αVβ6 SM ligand conjugated tool siRNA targeting PPIB in A549 cells as compared to naked siRNA. The alveolar organoids on the other hand, displayed a clear upregulation of MMP7 mRNA and protein response to a cocktail of profibrotic mediators highlighting the advantage of a more complex in vitro system. However, no clear differentiation in knockdown was observed between naked and αVβ6-ligand conjugated siRNA in alveolar organoids, likely due to the complexity of this system. We believe that this can be addressed via further optimization and addition of later time-points.

Keywords: Oligonucleotide Therapy, RNAi, siRNA, Integrin, avb6, Idiopathic Pulmonary Fibrosis, Fibrosis, MMP7, Assay Development, In Vitro Analysis, Gene Expression, mRNA, qPCR, Immunofluorescence Imaging, ELISA Assay, Cell Culture, 16HBE, A549, iPSC-derived Alveolar Organoids

Aims

In this thesis, our goal was to develop an in vitro biological effect assay as a proof-of-concept for αVβ6-targeted delivery of siRNA cargo in lung epithelium. To achieve this goal, we aimed to develop an assay in which an αVβ6 SM-ligand conjugated siRNA targeting the fibrotic mediator MMP7 linked to idiopathic pulmonary fibrosis (IPF) could be deployed. To that end, we evaluated different cell assay systems for their potential to secrete MMP7 in response to proinflammatory and profibrotic mediators. In addition, we investigated the applicability of αVβ6-ligand conjugated siRNA of each respective assay system by assessing the uptake and knockdown efficiency of an SM-conjugated tool siRNA targeting the housekeeping gene product *PPIB*.

Introduction

1. Oligonucleotide therapy

Oligonucleotides are short synthetic nucleic acid polymers engineered to bind to specific RNA or DNA sequences, utilizing endogenous cellular pathways to modulate the gene expression of disease-causing proteins. Oligonucleotides are divided into four major categories based on mode of action: Antisense oligonucleotides (ASOs), small interfering RNAs (siRNAs), small activating RNAs (saRNA) and aptamers. In contrast to small molecule drugs, oligonucleotide therapeutics allow for modulating the expression of proteins at mRNA level, significantly broadening the druggable target space. Based on a validated sequence of a disease-causing gene, oligonucleotide therapeutics can be rationally designed, significantly reducing the time and costs associated with screening big libraries of small molecules for hits and the subsequent chemical optimisation (Roberts, Langer, & Wood, 2020) (Moumné, Marie, & Crouvezier, 2022).

siRNA belongs to a class of oligonucleotides that utilizes the endogenous RNA interference (RNAi) pathway to inhibit protein expression before its corresponding mRNA transcript is translated. RNAi is a post-transcriptional gene silencing mechanism, carried out by short double-stranded RNA (typically 20-25 nucleotides) capable of mediating degradation of target mRNA. The siRNA sequences consist of a passenger (sense) strand and a guide (antisense) strand, which is complementary to the target mRNA transcript. Upon cell entry, the siRNA colocalizes with the RNA-induced silencing complex called RISC in the cytosol, followed by the discarding of the passenger strand. The guide strand then hybridizes with the target mRNA which triggers a nucleolytic degradation of the transcript by the argonaut-2 (AGO2) protein in the RISC complex (Figure 1). siRNA induced mRNA degradation is a powerful and precise tool for targeting transcripts of interest, making it an incredibly versatile tool in development of novel therapeutic applications (Roberts, 2015).

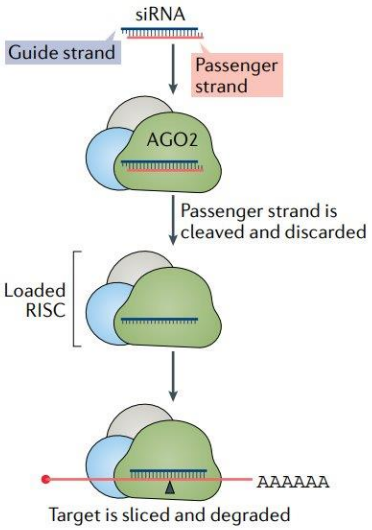

Figure 1. Mechanism of siRNA-induced gene silencing. siRNA is loaded into the RISC complex, followed by cleavage of the passenger strand. The loaded RISC complex binds to the target complementary mRNA sequence via Watson-Crick base paring of the guide strand. AGO2 protein in the RISC complex then cleaves the transcript, effectively silencing the gene. Adapted from "Advances in oligonucleotide drug delivery", by Thomas C. Roberts et al., 2020, nature reviews drug discovery, 19, p. 673-694 (https://doi.org/10.1038/s41573-020-0075-7)

While siRNA therapeutics offer superior target engagement compared to traditional small molecules, achieving effective tissue specific exposure and intracellular delivery remains a major translational challenge. Oligonucleotides are large hydrophilic molecules that cannot passively cross the plasma membrane as opposed to small molecule therapeutics. Internalization of siRNAs occurs through various endocytic pathways. Upon uptake, siRNA is taken across the cell membrane and into the cytoplasm in vesicles that are called the early endosomes. These mature into late endosomes and lysosomes, in which a portion of the cargo is released into the cytoplasm and the rest is degraded. To reach a therapeutic effect, the siRNA cargo needs to escape the endosomes into the cytosol before lysosomal degradation. Endosomal escape is a major bottleneck in maximizing therapeutic efficacy, as approximately 99% of the siRNA cargo fails to reach the target (Dowdy, 2023) (Roberts, Langer, & Wood, 2020). The administration route for siRNA delivery also has a significant effect on efficacy. With oral or intravenous administration, the majority of siRNA accumulates in the liver and is rapidly cleared by the renal system, which further complicates target delivery (Huang, et al., 2011). Local delivery is therefore the preferred administration route in which systemic exposure, hepatic uptake and first-pass metabolism is largely avoided.

Absorption, distribution, metabolism and excretion (ADME) of oligonucleotide drugs are very important parameters to consider. Strategies to improve delivery, stability and reduced immunogenicity all involve chemical modifications of different parts of the oligonucleotide. siRNA backbone modifications, most commonly addition of phosphorothioate (PS) linkages, increases the siRNAs half-life and enhances bioavailability. However, often several modifications are needed to reach the desired drug target profile, such as ribose sugar substitutions that improves target affinity and reduces immunogenicity. Uptake, delivery and specificity can be enhanced by attaching ligand conjugates tailored to bind specific cell surface receptors. Ligand conjugates can be lipids, small molecules, peptides or antibodies, further increasing the adaptability of siRNA oligonucleotide therapeutics. Since conjugation improves efficacy, the same therapeutic effect can be achieved with lower doses, which reduces off-target effects and potential siRNA-induced toxicity (Roberts, Langer, & Wood, 2020).

1.1 αVβ6 integrin as a receptor for targeted siRNA delivery in the lung

The human respiratory system can be divided into two main areas. The conducting airways are responsible for moving air in and out of the lung. Actual gas exchange occurs in the distal areas of the lung, which is comprised of millions of alveoli. Alveolar type 1 epithelial cells (AT1) constitute the major structure of the alveolar septum, with type 2 epithelial cells (AT2) spaced in between. AT1 cells maintain a barrier and are involved in the gas exchange, while AT2 cells are responsible for maintaining proper surface tension in the alveoli through production of surfactant proteins. AT2 cells are also progenitors of AT1 cells and play an integral part in lung regeneration and repair. Amongst other cells, fibroblasts and alveolar macrophages work together with AT2 cells to maintain lung homeostasis (Olajuyin, Zhang, & Ji, 2019).

Integrins constitute a major family of transmembrane adhesion receptors, responsible for the interactions between cells and the surrounding extracellular matrix (ECM) structures. They are heterodimeric glycoproteins consisting of an α- and a β- subunit, with a variety of isoforms that form 24 known combinations. The fundamental function of integrins in most species is to anchor the cytoskeleton of the cell to the ECM. However, integrins are also involved in a plethora of complex and very crucial signalling pathways that maintain and regulate important cell functions, including cell differentiation, proliferation, apoptosis, cell migration and intercellular communication. Integrins enable cells to adapt to changes in the extracellular environment (outside-in signalling) and influence the extracellular environment (inside-out signalling). Additionally, integrins including αVβ6-integrin, are important regulators of tissue homeostasis via the activation of the regulatory cytokine, TGF-β. αVβ6-integrin is predominantly expressed by epithelial cells in various organs, including the lung, skin, liver, and kidney. In the lung, αVβ6-integrin is expressed by both bronchial and alveolar epithelial cells (Slack et al., 2022) (Saini, et al., 2015). The expression of αVβ6 receptors is low in healthy lung epithelium; however, significant elevation in αVβ6 levels have been associated with many pathological conditions, including IPF (Decaris, et al., 2021) (Bandyopadhyay & Raghavan, 2009) (Slack et al., 2022). Due to their diverse role and involvement in various cancers and fibrotic diseases, integrin-targeted therapies have gained significant attention in the preclinical and clinical space. Current clinical trials feature small molecules, peptides or antibodies that block integrin receptors. αVβ6 Integrin has also been investigated for receptor-mediated delivery of therapeutic payloads used to target various disease-associated genes in the lung epithelia with high precision, including siRNA. These contain peptide or small molecule conjugations that mimic αVβ6 ligands, taking advantage of the epithelial-specific expression pattern and good receptor recycling characteristics. Arrowhead Pharmaceuticals have several ongoing clinical trials featuring αVβ6-targeted ligand-conjugated siRNA targeting key genes involved in the pathophysiology of IPF (Arrowhead Pharmaceuticals, 2023) (Arrowhead Pharmaceuticals, 2022) (United States of America Patent No. US-20190248832-A1, 2019), confirming their therapeutic potential.

2. Idiopathic Pulmonary Fibrosis

Idiopathic pulmonary fibrosis, or IPF, is a progressive chronic lung disease that affects 10-20 out of 100 000 people worldwide. IPF causes rapid decline in lung function, characterized by progressive replacement of healthy lung tissue surrounding the alveoli with stiff, fibrotic scars. The disease mainly affects individuals aged 50 and older, with an average life expectancy of 3-5 years post-diagnosis. Symptoms manifest as shortness of breath, extreme tiredness, excessive coughing, and abnormal weight loss. It is not yet known what causes IPF, and the absence of early, accurate diagnostic tools, reliable disease prediction models and effective regenerative therapies presents a significant barrier to advancing treatment strategies and improving the quality-of-life for IPF patients (Idiopathic pulmonary fibrosis, 2020) (Glass, et al., 2022) (Mei et al. 2022) (Sgalla, et al., 2018) (Richeldi, Collard, & Jones, 2017). Currently, the only two FDA-approved antifibrotic drugs Pirfenidone and Nintedanib slow down disease progression, but fail to reverse fibrosis. Regarding non-pharmacologic therapies, only lung transplantations currently provide potential improvement of survival rates, albeit with many risks and complications involved in addition to limited number of donors (Zhao, et al., 2022).

2.1 Pathophysiology of IPF

The cause of IPF is not clearly understood compared to other types of fibrotic lung diseases. Environmental factors such as long-term exposure to pollution, cigarette smoke and occupational dust have been shown to play a significant role. Factors such as telomere shortening-induced DNA damage and cell senescence of AT2 cells, endoplasmic reticulum stress, damaged mitochondria and increase in reactive oxygen species have also been linked to dysfunctional re-programming of the healing process that leads to chronic accumulation of fibrotic scars in the lungs (Zhou, Ling, & Shi, 2024) (Henderson, Rieder, & Wynn, 2020) (Distler, et al., 2019) (Heukels, Moor, Von Der Thüsen, Wijsenbeek, & Kool, 2019) (Courtwright & El-Chemaly, 2019). The current consensus is that IPF is characterized by chronic injury and dysregulated and pathological wound healing (Zhang & Wang, Cellular and Molecular Mechanisms in Idiopathic Pulmonary Fibrosis, 2023).

Tissue repair and regeneration in healthy lungs are characterized by well-coordinated cellular processes that culminate in restoring the lung architecture following injury. In broad terms, healing occurs in three main stages: inflammation, re-epithelization and resolution of scar tissue that formed as a result of wound repair. Upon injury, damaged epithelial cells release damage-associated molecular patterns (DAMPs). DAMPs in turn bind to the pattern recognition receptors (PRRs) expressed by epithelial cells and macrophages, activating key parts of the coordinated immunoinflammatory response in the lungs. Upon activation of PRRs, various proinflammatory and profibrotic mediators such as interleukins, metalloproteinases (notably MMP7), transforming growth factor β (TGF-β), platelet-derived growth factors (PDGF), Tumour necrosis factor α (TNF-α) are released at the site of injury. Cytokines and chemokines will recruit and activate neutrophils, monocytes and lymphocytes to the lung which further propagates the inflammatory response, marking the acute inflammatory phase. Profibrotic mediators then initiate re-epithelization and wound closure. Re-epithelization is supported by fibroblasts (activated fibrocytes) through production of ECM-scaffolds. Fibroblasts are responsible for maintaining lung tissue homeostasis and integrity through attenuation of the produced levels of ECM. When injury occurs, a portion of the recruited and activated fibroblasts further differentiate into myofibroblasts in response to the release of the various aforementioned mediators. Myofibroblasts in turn produce significant amounts of collagen-rich ECM that helps with contraction of the wound. The proinflammatory response subsides during the end-stage of healing, characterized by replenishment of damaged epithelia and formation of temporary scars. Myofibroblasts are cleared from the injury site via apoptosis, minimizing scar tissue formation. The localized scars are then resolved by metalloproteinase-mediated ECM degradation pathways, restoring the normal tissue function. In IPF however, these processes are dysregulated, where persistent and increased secretion of inflammatory and pro-fibrotic mediators as well as impaired clearance of ECM-producing cells leads to excessive deposition of ECM components rather than proper wound repair (Figure 2). Accumulation of fibrotic scars constitutes a complex positive feedback-loop between various pathways and cell types. It is supported by the observed increase in profibrotic macrophage population which further maintain the release of fibrotic mediators and inhibit the differentiation of AT2 cells into AT1 cells, a process crucial for obtaining lung injury repair and return to homeostasis. (Zhou, Ling, & Shi, 2024) (Henderson, Rieder, & Wynn, 2020) (Distler, et al., 2019) (Heukels et al., 2019) (Franzén, et al., 2024) (Zhou et al., 2024).

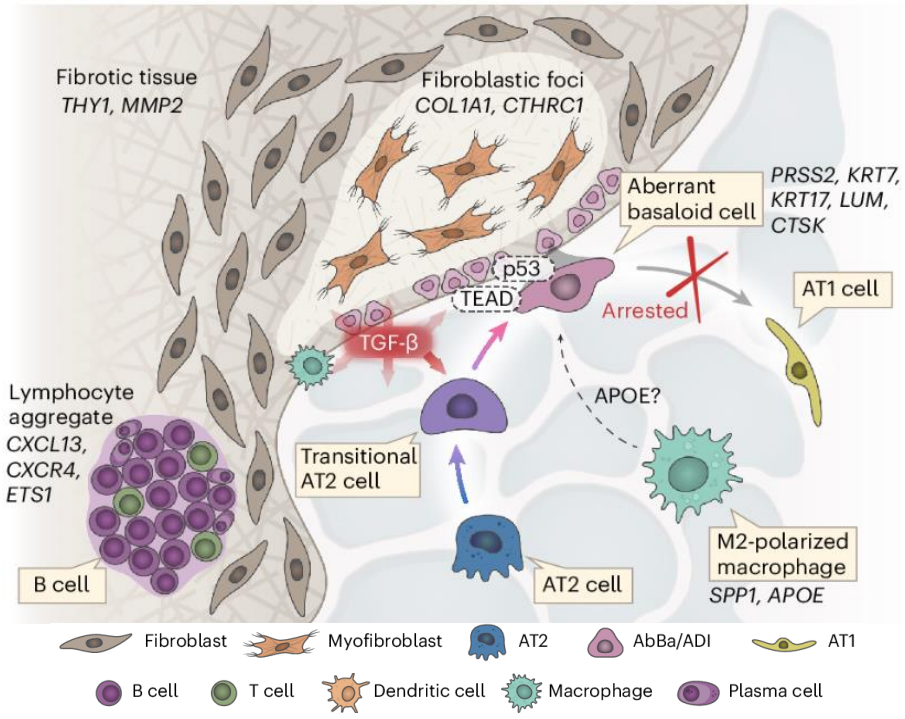

Figure 2. Overview of IPF pathophysiology in human alveolar microenvironment, illustrating the dysregulated healing process at the leading edge of fibrogenesis. TGF-β, and several other cytokines and chemokines, drive the formation of partially differentiated AT2 cells that express EMT-like phenotypes. TGF-β as well as other inflammatory mediators (not shown) also recruit and activate fibroblasts, leukocytes and myofibroblasts at the site of injury, forming dense areas called the fibroblastic foci which are regions of active fibrogenesis. Due to disrupted homeostasis of the alveolar space, the fate of EMT-like AT2 cells is altered, characterized accumulation of alveolar differentiation intermediates (ADI), also called aberrant basaloid cells. ADI cells and constitutively activated myofibroblasts lead to excessive deposition of ECM, as the tissue attempts to heal itself while being unable to properly resolve the injury. Ultimately this leads to a continuous loss of AT1 cells and remodelling of the alveolar architecture. Adapted from "Mapping spatially resolved transcriptomes in human and mouse pulmonary fibrosis", by Franzén et al., 2024, Nature Genetics, 56, p. 1725–1736 (https://doi.org/10.1038/s41588-024-01819-2)

A core contributor to fibrogenesis and tissue remodelling in IPF is the presence of defective epithelial cell expressing aberrant basaloid cell phenotype. As part of re-epithelization during wound healing, AT2 cells undergo a process called partial epithelial-mesenchymal transition (EMT) in which the cells assume a more mesenchymal phenotype (Figure 3). This phenotype is characterized by increased mobility, where the cells shed from their attachment to the ECM. EMT is generally a reversible process, it mediates early wound healing and tissue remodelling by promoting re-epithelialization of the local site of injury. In IPF, the population of AT2 cells that have undergone partial EMT (as they still clearly exhibit an array of epithelial cell features) is significantly increased. These cells are referred to as alveolar differentiation intermediates (ADI), expressing so called aberrant basaloid phenotype characterized by the expression of markers such as keratin-17 (KRT17) (associated with damaged AT2 cells and improper differentiation), vimentin (VIM) (responsible for increased cellular integrity and motility), smooth muscle actin alpha (ACTA2 or α-SMA) (producing contractile actin fibres in ADI cells) and loss of surfactant protein C (SPC) expression, an AT2 cell marker. Furthermore, ADI cells are found in dense fibrotic regions called the fibroblastic foci, which are considered sites of active fibrogenesis (Yamaguchi, et al., 2016). The most notable pathways involved in these processes are TGF-β signalling, Wnt/β-catenin and the Sonic Hedgehog pathways that regulate the various differentiation processes in wound healing (Akhmetshina, et al., 2012) (Effendi & Nagano, 2022).

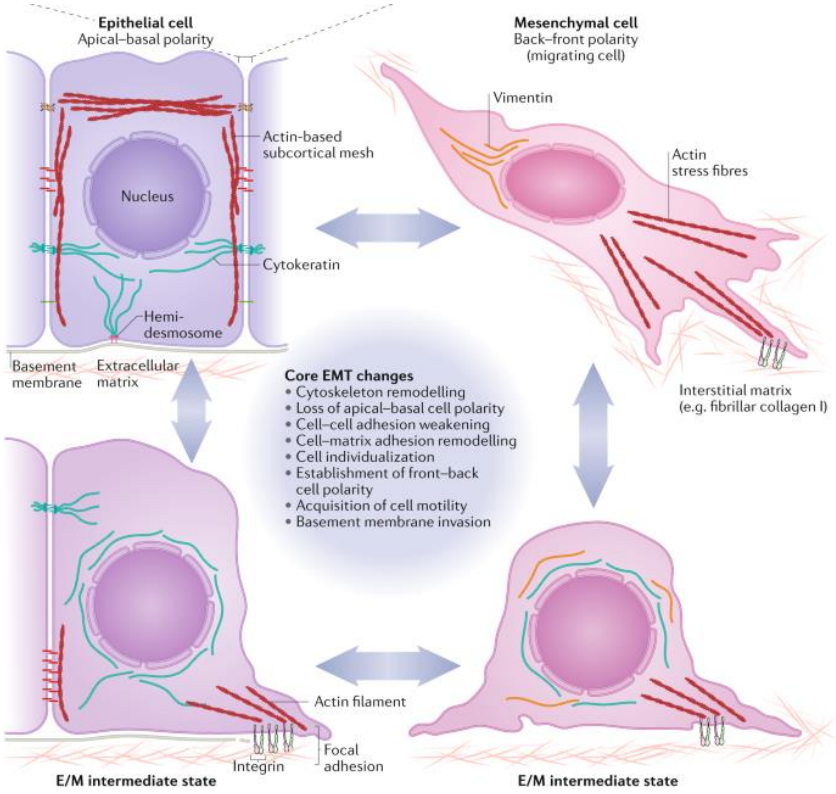

Figure 3. Overview of epithelial to mesenchymal transition (EMT). Epithelial cells have precise shapes that are maintained by various cell junctions. During EMT, upregulation of vimentin (VIM) and actin stress fibres such as ACTA2 changes the morphology of the cell. Where epithelial cells attach in tight clusters, the mesenchymal intermediates gain motility and can migrate to the site of injury. Adapted from "Guidelines and definitions for research on epithelial–mesenchymal transition", by Jing Yang et al., 2020, Nature Reviews Molecular Cell Biology, 21, p. 341-352 (https://doi.org/10.1038/s41580-020-0237-9)

TGF-β is a core mediator in a diverse array of cancer and fibrotic diseases and is linked to many important functions such as inflammation, immune responses, wound healing, cell growth and cell differentiation. Due to the multifunctional role of TGF-β in physiological conditions, it has been at the centre of IPF research. In this context, significantly elevated levels of TGF-β are associated with epithelial injury, inflammation, differentiation of AT2 cells and acquisition of aberrant basaloid phenotype, abnormal activation and accumulation of myofibroblasts and ECM remodelling. TGF-β is present as inactive latent complexes which can be activated in several ways, notably by integrins that mechanically release the active TGF-β from its complex. αVβ6 integrin, which is epithelial restricted and highly overexpressed in IPF lungs, contributes to the significant increase of active TGF-β observed in both animal models of IPF and IPF patients. To that end, attenuation of the TGF-β signalling pathways through targeting of the αVβ6 integrin have shown promising results in treatment of fibrosis in mouse models of lung fibrosis (Horan, et al., 2007) (Deng, et al., 2024) (Zhao, et al., 2022).

Matrix metalloproteinases (MMPs) are involved in ECM degradation, release of growth factors bound in the ECM (notably release of TGF-β), cell migration (through E-cadherin cleavage) (McGuire, Li, & Parks, 2003), activation of AT2 cells, neutrophil recruitment (Gill, et al., 2016) and therefore, involved in aberrant extracellular remodelling in fibrotic diseases. It is important to note that MMPs have both antifibrotic and profibrotic properties. However, MMP7 in particular, with its broad substrate specificity, has been recognized as a key contributor to ECM remodelling in IPF. Levels of MMP7 in samples obtained from IPF patients and *in vivo* IPF models were significantly elevated (Craig et al., 2015) (Pardo et al., 2016). Bleomycin-induced fibrosis (most widely used and best characterized murine IPF model) was significantly reduced in MMP7-deficient mice compared to wild type mice , further signifying the role of MMP7 as a profibrotic mediator in IPF (Zuo, et al., 2002). In a paper published by McGuire et al (2003), the authors postulated that MMP7 can promote EMT in addition to the Wnt/β-

catenin pathway (Sun, Xing, Zhou, Song, & Gao, 2024) via mediating the surface-shedding of E-cadherin in the E-cadherin/β-catenin complex. This complex constitutes part of the tight junctions between epithelial cells, similar to integrins. As a result of E-cadherin surface shedding, the intracellular β-catenin dissociates and is transported to the nucleus, where it interacts with transcription factors regulating the expression of mesenchymal markers, promoting partial EMT. MMP7 also contributes to recruitment of inflammatory leukocytes via cleavage of the murine syndecan-1 (ortholog to human interleukin-8) transmembrane protein on the surface of epithelial cells, in turn creating a chemical gradient that guides the leukocytes to the site of injury (Gill, et al., 2016) (Swee et al., 2008). Additionally, significantly elevated MMP7 levels in IPF lead to degradation of ECM components, destroying the basement membrane that supports epithelial cells. This degradation is linked to increased cell motility and invasiveness in many cancer diseases and similarly, contributes to cell migration and aberrant basaloid cell formation in IPF (Chen, et al., 2023) (Han, et al., 2015). These mechanisms highlight the complex interplay and the self-reinforcing nature of MMP7-mediated fibrogenesis in IPF. MMP7 expression in IPF can be induced by TGF-β, Wnt/β-catenin signalling pathway and osteopontin, a protein shown to be involved in accelerating IPF progression (Pardo, et al., 2005) (White, et al., 2016). Research indicates that MMP7 can be used as potential biomarker and prognostic marker for IPF severity and interstitial lung diseases (Rosas, et al., 2008). Of note, Arrowhead Pharmaceuticals have ongoing phase I and phase IIa clinical trials of a small molecule αVβ6-ligand conjugated siRNA targeting MMP7 (Arrowhead Pharmaceuticals, 2023), highlighting the potential of MMP7 as a therapeutic target for IPF (ClinicalTrials.gov., NCT05537025).

Results

1. Stimulation of 16HBE cells with lipopolysaccharide and tumour necrosis factor failed to induce *MMP7* upregulation

αVβ6-integrin targeted siRNA has been successfully delivered in the human bronchial epithelial cell line, 16HBE, and target engagement with the tool siRNA, targeting the housekeeping gene *PPIB*, has been validated for both naked and SM conjugated siRNA (data generated previously in house, not shown). The tool siRNA used in this system targets *PPIB*, a housekeeping gene that is not related to IPF or any other major pathophysiology. Therefore, we attempted to develop an *in vitro* biological effect assay in which a siRNA cargo directed towards a more functional target, rather than a housekeeping gene would be delivered to the cells. To this end, siRNA targeting *MMP7* was selected. Upon proinflammatory stimulation, *MMP7* was reported to crucially contribute to the release of the major neutrophil chemoattractant, *CXCL8* (or *IL8*), by epithelial cells via cell surface shedding of the chemokine (Gill, et al., 2016). Therefore, we first evaluated the inflammatory reaction of 16HBE cells in response to lipopolysaccharide (LPS), a cell wall component of gram-negative bacteria that induces potent immunoinflammatory responses in cells. 16HBE lysates were assessed for expression of *MMP7*, interleukin 6 (*IL6*) and interleukin 8 (*IL8*), which are common inflammation markers. Actin Beta (*β-actin*) and hypoxanthine phosphoribosyl transferase (*HPRT*) genes were used as normalization controls for qPCR.

Gene expression was evaluated at 24, 48 and 72h after LPS stimulation. *MMP7* expression was upregulated approximately 2-fold in cells 48h post-treatment with 0.63 µg/mL LPS, and 1.30-fold in cells treated with 1.25 µg/mL as compared to vehicle (PBS) (Figure 4). The expression however was back to baseline after 72h. No increase (or decrease) was observed for the other LPS concentrations. Furthermore, the *IL6* and *IL8* data showed a clear inflammatory response, as seen by an acute increase in fold-change 24h post-treatment. The expression levels went back to baseline at later time-points. As these results indicate that the overall proinflammatory response to LPS was rather weak, we investigated another proinflammatory stimulus, namely TNF-α.

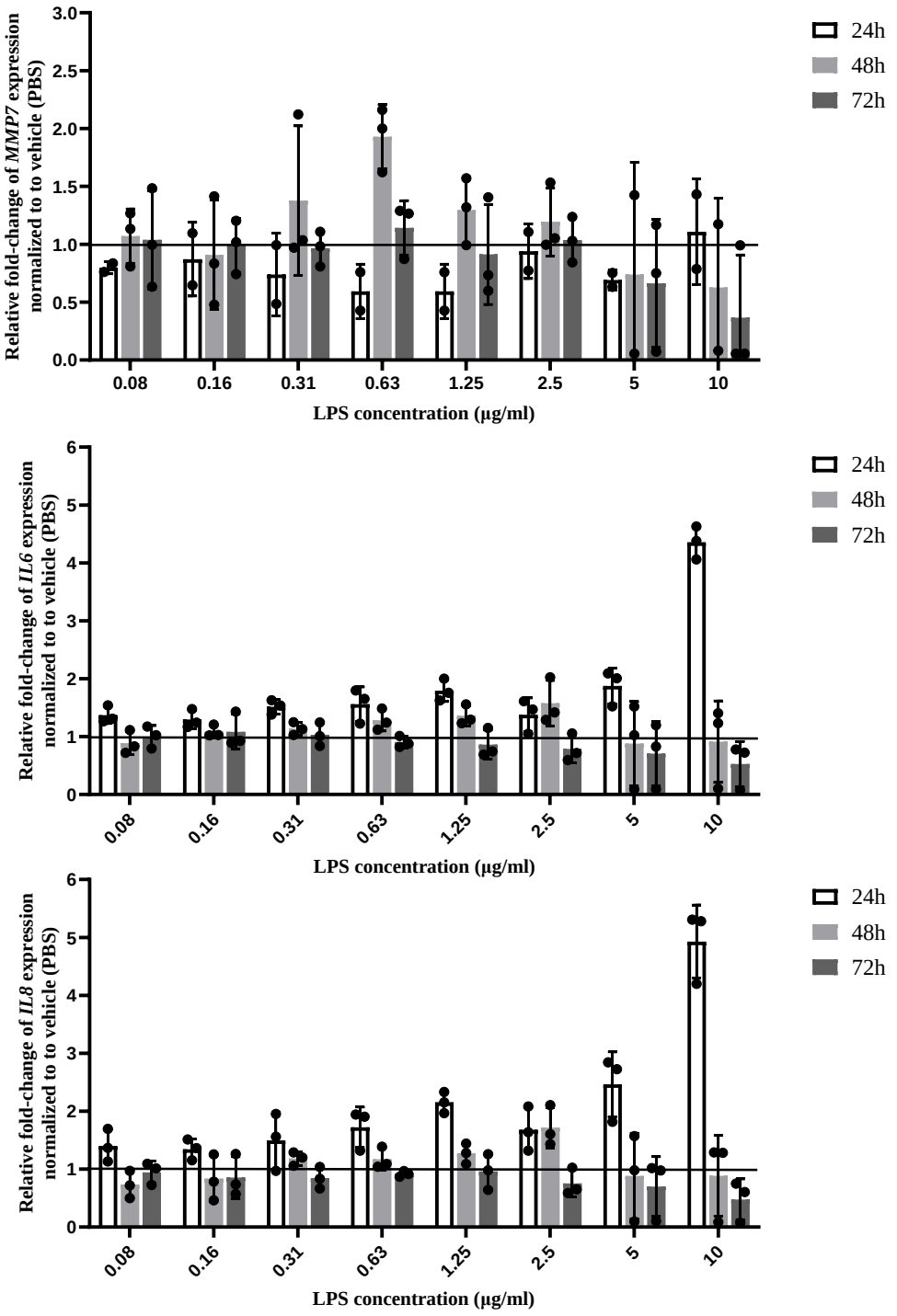

Figure 4. Gene expression data showing the fold-change in MMP7, IL6 and IL8 mRNA expression relative to vehicle (PBS), 24h, 48h and 72h post-treatment with LPS. The time- and dose-dependent upregulation of IL6 and IL8 indicated an early inflammatory response that was back to baseline in later time-points. The overall MMP7 gene expression however was not significantly affected by LPS.

The inflammatory reaction of 16HBE cells in response to TNF-α stimulation was evaluated at 6 and 24h post-treatment with the designated concentrations (Figure 5). Since LPS induced an overall weak inflammatory response in 16HBE, TNF-α was chosen as a downstream surrogate of LPS, due to higher expression of its cognate receptors in epithelial cells. To that end, earlier time-points were chosen as TNF-α induces a more potent inflammatory response in epithelial cells compared to LPS. TNF-α did not induce a clear upregulation of *MMP7* gene expression, whereas *IL6* and *IL8* were upregulated at higher concentrations, indicating an inflammatory response albeit lower than LPS. Together, these data indicate that both LPS and TNF-α induce a rather weak inflammatory response in 16HBE cells, which did not translate into an upregulation of *MMP7* gene expression.

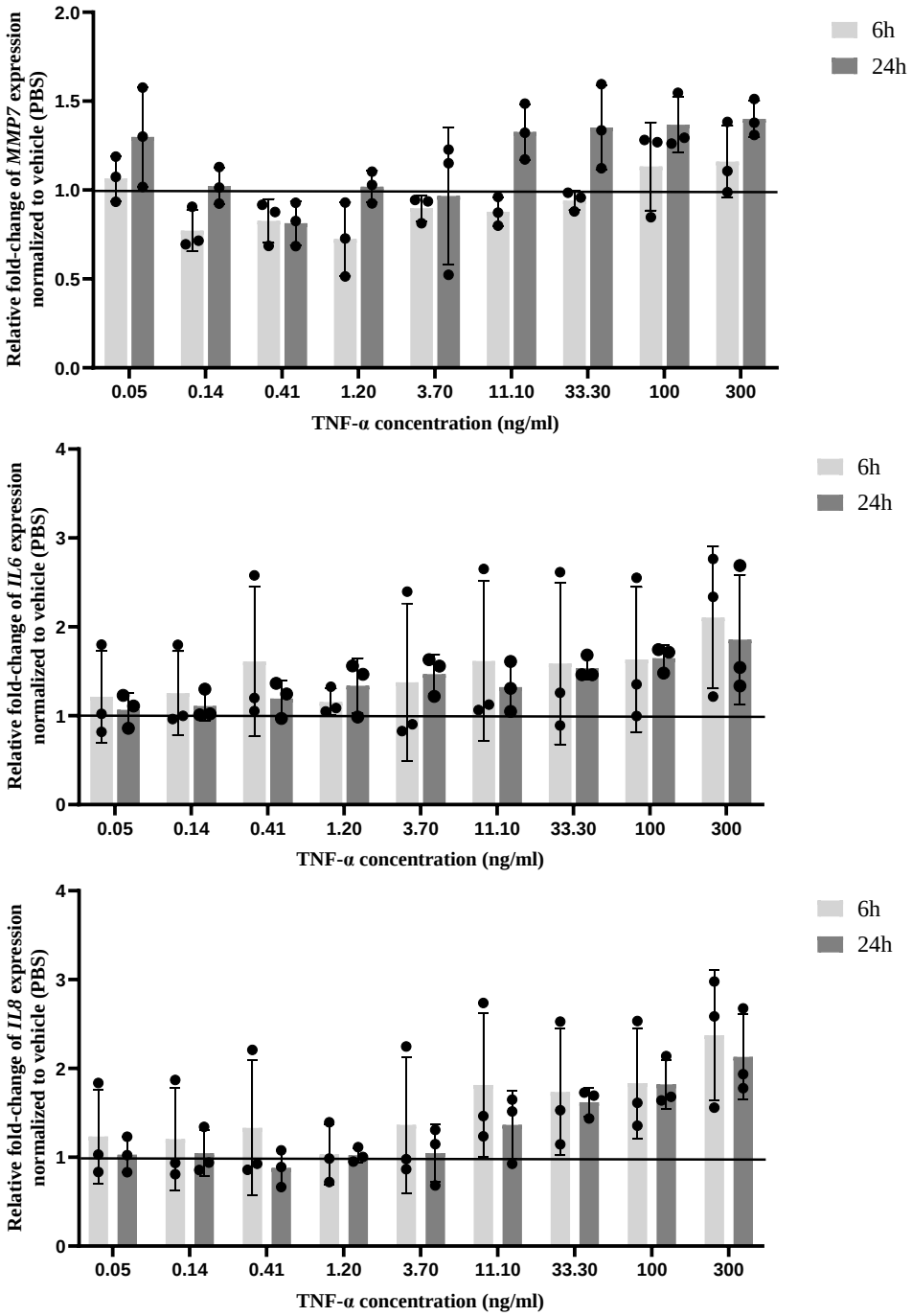

Figure 5. Gene expression data showing the fold-change in MMP7, IL6 and IL8 mRNA expression relative to vehicle (PBS) at 6h and 24h after TNF-α stimulation. Similar to stimulation with LPS, early upregulation of IL6 and IL8 indicate an acute inflammatory response that went back to baseline at later time-points. The overall MMP7 gene expression however was not significantly affected by TNF-α.

2. Delivery of αVβ6-targeted siRNA and modelling fibrosis induces epithelial damage in human adenocarcinoma epithelial cell line

MMP7 plays a key role in neutrophil recruitment and this protein is actively secreted by epithelial cells in response to external stress. However, this was not translated into the 16HBE model, as neither the *MMP7* nor the inflammatory cytokines *IL6* and *IL8* were significantly induced upon treatment with LPS and TNF-α. We therefore decided to shift our focus towards the human adenocarcinoma epithelial cell line A549. A549 cells have been widely used to model alveolar type II (AT2) epithelial cells and are frequently utilized to study the pathophysiology of various lung diseases, including IPF. Unlike 16HBE cells, which express common genetic markers similar to proximal epithelial cells in the airway system, A549 cells better match the genetic patterns of alveolar epithelial cells (distal region of the lower respiratory tract) and are successfully used in numerous studies to develop EMT/fibrosis assays.

2.1 Surface expression of αVβ6-integrin is low in A549 in comparison to 16HBE

One of the key requirements of a biological effects assay for evaluating αVβ6-integrin targeted siRNA is the presence and quantity of surface αVβ6 expression. To this end, we quantified the surface expression of αVβ6 integrin in A549 cells in comparison to 16HBE via immunofluorescence (IF) imaging. This was done by staining A549 with an antibody recognizing the b6-subunit of the αVβ6 heterodimer. 16HBE cells were used as a comparison/positive control for the staining. Although significantly lower compared to 16HBE cells, A549 cells showed clear αVβ6 integrin surface expression (Figure 6). Comparing the average mean fluorescent intensity (MFI) signal of αVβ6 integrin, it was approximately 38-fold lower in A549 than 16HBE. Nevertheless, clear expression of αVβ6 in the A549 cells meant that the cell line fulfilled the minimum requirement for subsequent experiments.

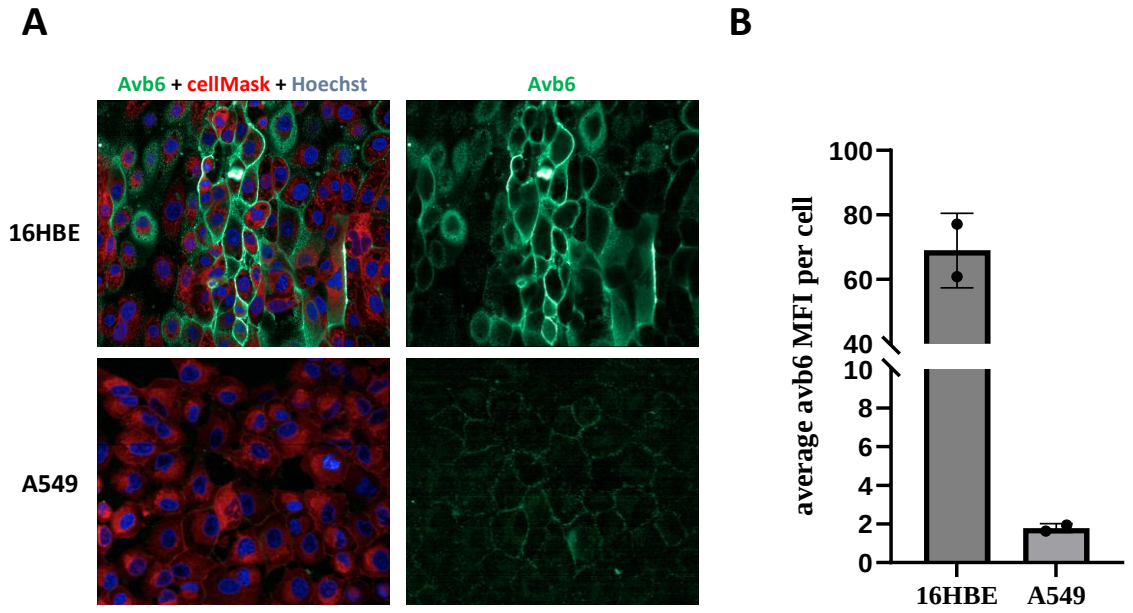

*Figure 6. Surface expression of αVβ6 measured via IF imaging. **A**, the signals are visualized for αVβ6 (green), cellMask (red) and Hoechst (blue). αVβ6 signal is provided separately (due to low signal intensity) to show the presence of αVβ6 signal in A549 cells. **B**, the mean αVβ6 fluorescence intensity (MFI) signal is provided with the background signal (unstained control) subtracted. The MFI was calculated as average of all cells per well, for two wells in total. The surface expression of αVβ6 was approximately 38-fold lower in A549 cells compared to 16HBE cells.*

2.2 αVβ6 SM-ligand conjugated siRNA induces increased PPIB knockdown in A549 cells as compared to naked siRNA

The uptake and knockdown (KD) efficiency of the αVβ6-ligand conjugated siRNA is dependent on the αVβ6 surface expression and internalization. To this end, we wanted to confirm whether the observed αVβ6 surface expression in A549 cells would be sufficient to obtain efficient delivery and KD induced by an αVβ6-ligand conjugated siRNA. Therefore, we used the small molecule (SM) αVβ6-ligand tool developed by Arrowhead Pharmaceuticals, which targets the RGD binding site of the αVβ6 complex. To evaluate the KD efficiencies of both unconjugated (naked) and SM-conjugated PPIB siRNA in A549 cells, two proof-of-concept (POC) dose-response gene expression experiments were performed at 48h and 72h time-points. The study utilized a designated range of siRNA concentrations, as illustrated in Figures 7 and 8. Positive controls were included by transfecting A549 cells with PPIB siRNA using Lipofectamine RNAiMAX reagent, a well-established method for RNA interference experiments. A549 lysates were analysed for PPIB expression, using succinate dehydrogenase complex subunit A (*SDHA*) and hypoxanthine phosphoribosyltransferase (*HPRT*) as house-keeping genes for qPCR.

SM-conjugated *PPIB* siRNA induced 56.6% KD at 10 µM and 25.6% KD at 1 µM as compared to the vehicle control (PBS) 48h post-treatment (Figure 7). The naked *PPIB* siRNA induced only 25% KD at 10 µM compared to vehicle control, whereas 1 and 0.1 µM concentrations did not induce any significant KD. Naked *PPIB* siRNA at max dose (10 µM) induced comparable KD to the 1 µM SM-conjugated siRNA, as compared to the vehicle control. Naked and SM-conjugated *PPIB* siRNA transfected with RNAiMAX induced approximately 97% KD as compared to vehicle control, while the SM ligand alone did not induce any KD. To summarize, Arrowhead's αVβ6-ligand tool increased the KD efficiency of the tool *PPIB* siRNA across all concentrations compared to the naked siRNA.

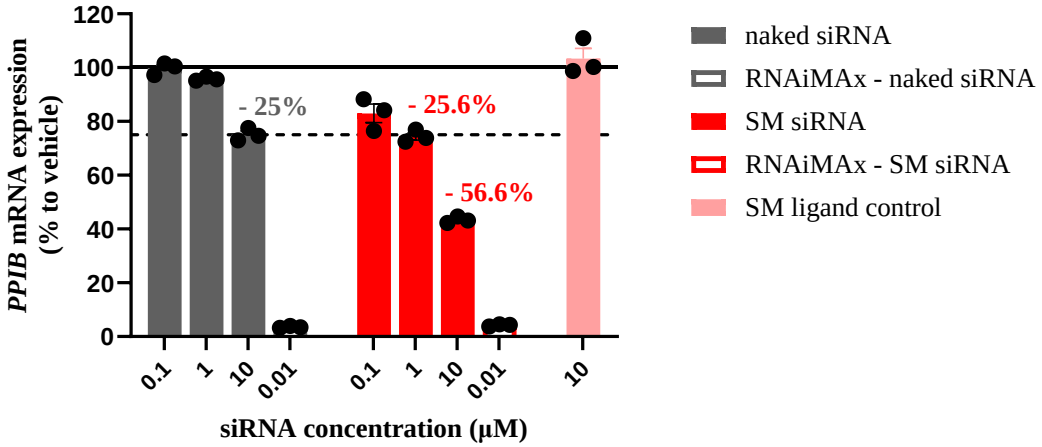

Figure 7. Gene expression data showing the dose-response KD 48h post-treatment. A549 cells were treated with 0.1, 1 and 10 µM of naked and SM-conjugated PPIB siRNA. Positive controls include transfection with 0.01 µM naked and SM-conjugated siRNA using RNAiMAX. Negative control includes treatment with the SM ligand alone (10 µM). The dashed line marks the maximum achieved KD (10 µM SM-conjugated siRNA). Naked siRNA at maximum dosage induced comparable KD as the 10-fold lower dose of the 1 µM SM-conjugated siRNA. The difference in KD between 10 µM SM-conjugated siRNA and naked siRNA equals to a percent change of +126.4%.

The dose-response is similar at 72h post-treatment. SM-conjugated *PPIB* siRNA induces 53.2%, 27% and 10% KD at 10 µM, 1 µM and 0.1 µM respectively compared to vehicle (Figure 8). The naked *PPIB* siRNA induces approximately 32% KD at 10 µM compared to vehicle control, whereas no knockdown could be observed at 1 and 0.1 µM. Naked *PPIB* siRNA at 10 µM induced comparable KD to the 1 µM SM-conjugated siRNA similar to the 48h time-point. Lipofectamine transfected naked and SM-conjugated *PPIB* siRNA induced 90% and 95% KD respectively. The SM ligand alone did not induce

any KD. Together, despite the relatively low surface expression of αVβ6 integrin, SM-conjugated *PPIB* siRNA clearly induced a dose-dependent, increased KD in A549 cells as compared naked siRNA.

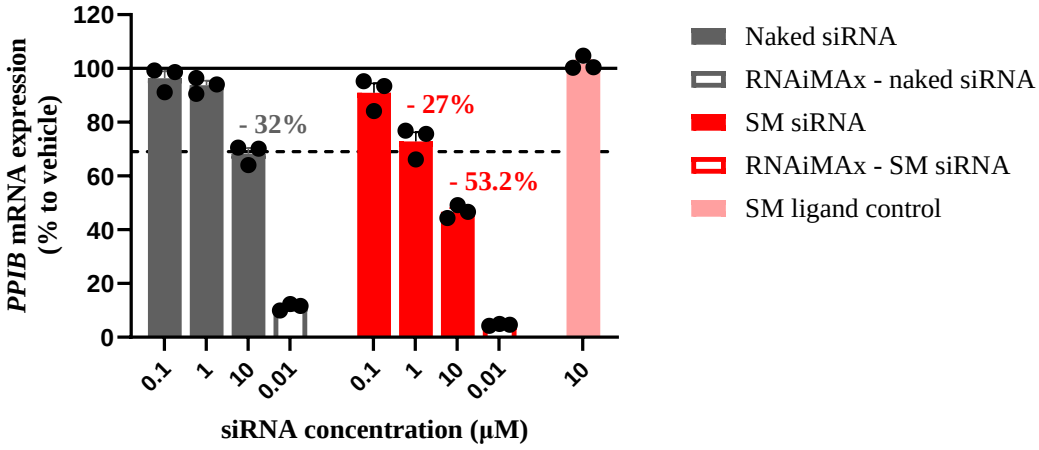

Figure 8. Gene expression data showing the dose-response KD 72h post-treatment. A549 cells were treated with 0.1, 1 and 10 µM of naked and SM-conjugated PPIB siRNA. Positive controls include transfection with 0.01 µM naked and SM-conjugated siRNA using RNAiMAX. Negative control includes treatment with the SM ligand alone (10 µM). The dashed line marks the maximum achieved KD (10 µM SM-conjugated siRNA). Naked siRNA at maximum dosage induced comparable KD as the 10-fold lower dose of the 1 µM SM-conjugated siRNA. The difference in KD between 10 µM SM-conjugated siRNA and naked siRNA equals to a percent change of +66.3%.

2.3 Increased uptake of SM-conjugated versus naked siRNA in A549 cells

To confirm that, as compared to naked siRNA, the increased *PPIB* KD induced by the SM-siRNA was due to increased intracellular delivery, uptake of naked and SM-conjugated PPIB siRNA was evaluated via imaging. A549 cells were treated with 1 µM of Alexa Fluor 647 labelled naked and SM-conjugated PPIB siRNA. A higher portion of SM-conjugated siRNA (red signal) colocalized in the cytoplasm of cells treated with SM-conjugated versus siRNA (Figure 9A). Average fluorescent intensity signal of SM-conjugated siRNA was increased ~4 fold compared to naked siRNA (Figure 9B).

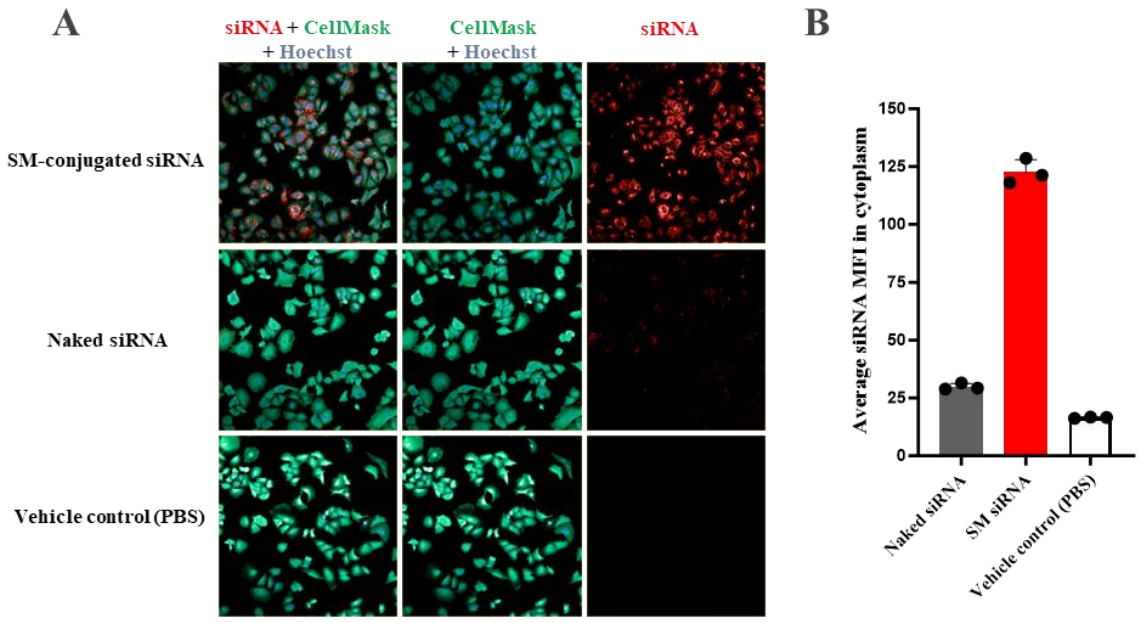

*Figure 9. **A**, Imaging results of the siRNA uptake in A549 cells, 6h post-treatment. Cells stained with Hoechst 33342 nuclear counterstain (blue) and CellMask plasma membrane stain (green). The SM-conjugated siRNA signal in the cytosol is significantly higher compared to naked siRNA. **B**, Average fluorescence intensity (MFI) signal of Alexa Fluor 647 labelled naked and SM-conjugated PPIB siRNA. Uptake via imaging was assessed 6h post-treatment, after fixation with 4% paraformaldehyde. The MFI signal of vehicle control (PBS) was included to quantify the background.*

2.4 Profibrotic stimuli upregulate epithelial-to-mesenchymal transition markers

In IPF, aberrant basaloid cells express some EMT-like markers and MMP7 is reported to be an important driver of this process (Chen, et al., 2023) (Pardo et al., 2016). To investigate induction of EMT-like phenotype and concurrent MMP7 expression, A549 cells were treated with various profibrotic compounds, including the StemXVivo EMT Inducing Media Supplement, recombinant human Osteopontin, TGF-β, a fibrotic cocktail (FC), TNF-α, platelet derived growth factor AB (PDGF-AB) and Lysophosphatidic acid (LPA). A549 cell lysates were analysed for the expression of *MMP7*, surfactant protein C (*SFTP-C*), vimentin (*VIM*), keratin-17 (*KRT17*), and smooth muscle α-2 actin (*ACTA2*). These markers are commonly associated with EMT, representing the phenotypic changes in epithelial cells as they transition to a more mesenchymal phenotype. During EMT, epithelial cells lose markers such as *SFTP-C*, while mesenchymal markers like *VIM*, *KRT17*, and *ACTA2* are upregulated.

Figure 10 presents the qPCR data following a 5-day stimulation with FC and StemXVivo. The results showed that, compared to the vehicle control, *MMP7* expression is surprisingly downregulated across all stimulation conditions, with the strongest effect observed in StemXVivo-treated cells. Similarly, *SFTP-C* expression was markedly reduced in response the FC and StemXVivo as compared to the vehicle control (PBS). In contrast, *VIM* and *KRT17* expression was upregulated in response to FC (only 1X and 0.1X condition for *KRT17*) and StemXvivo treatments. Notably, the StemXVivo treatment induced upregulation of *ACTA2*, which was not observed with the other treatments except for the 0.3X FC condition. These findings demonstrate that the EMT markers followed the expected expression patterns, with the StemXVivo treatment producing the most pronounced EMT-like response.

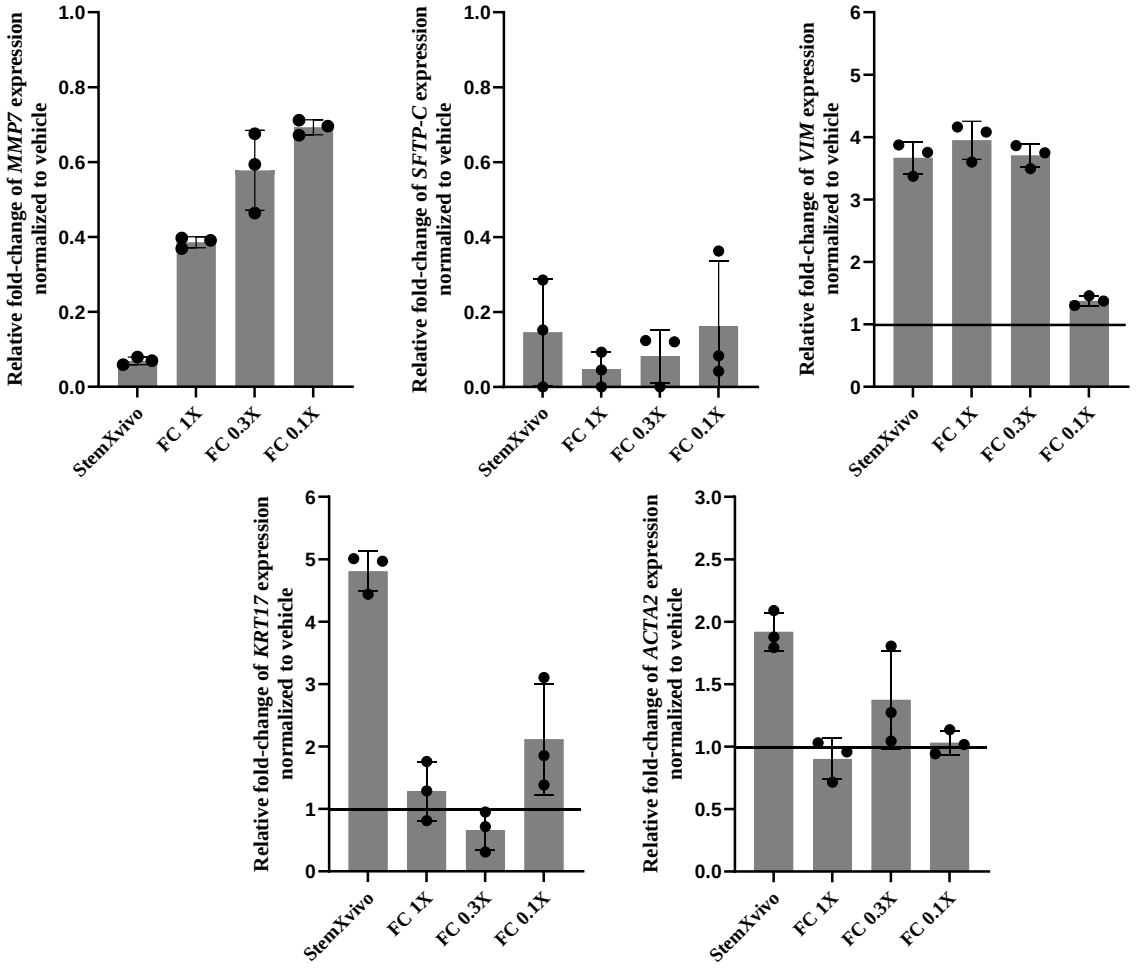

Figure 10. Gene expression data showing fold-changes in MMP7, SFTP-C, VIM, KRT17 and ACTA2 mRNA levels relative to vehicle (PBS), 5 days post-treatment with StemXVivo and fibrotic cocktail (FC). MMP7 mRNA expression was downregulated across all conditions, notably StemXVivo. The EMT markers confirm the transition of A549 cells to a more mesenchymal phenotype, with the StemXVivo producing the most pronounced EMT response.

We next wanted to see whether the downregulation of *MMP7* transcript translates to reduced protein levels. Total MMP7 protein content in supernatants was quantified via an ELISA assay. MMP7 protein was reduced approximately 3.5 fold in response to FC treatment, and completely absent after StemXVivo treatment (Figure 11). These results show that treatment with StemXVivo and FC reduces MMP7 both at the gene expression and protein level.

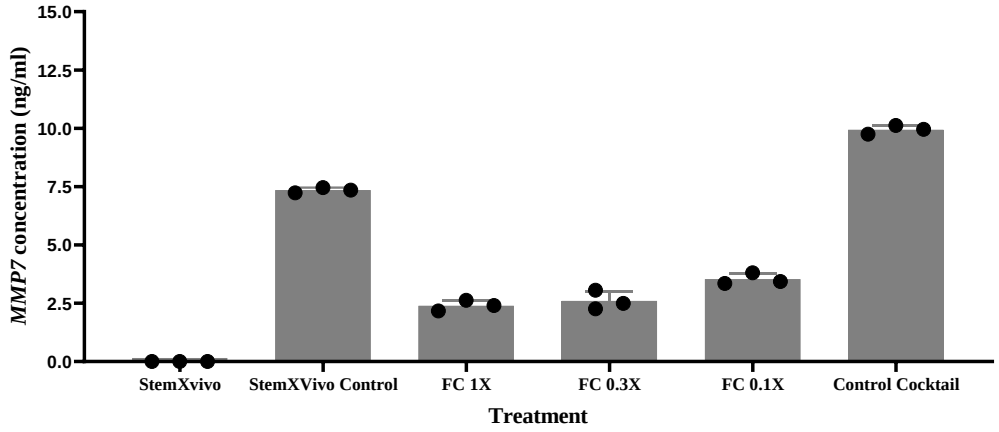

Figure 11. MMP7 concentration measured via ELISA in supernatants collected from A549 cells treated with StemXVivo and fibrotic cocktail, including the vehicle controls for each treatment respectively. Cells treated with StemXVivo Control received only PBS while cells treated with Control Cocktail received a mixture of the carrier solvents of the fibrosis compounds. See Materials and Methods for further detail. MMP7 protein concentration was significantly decreased across all conditions, as compared with the respective vehicle controls.

TGF-β is a key inducer of EMT and plays a key role in the upregulation of MMP7 as mentioned before. However, the significant downregulation of *MMP7* observed in the prior experiment led us to hypothesize that other components in the StemXVivo and fibrotic cocktail may have counteracted this effect. Additionally, it is possible that the peak *MMP7* expression occurred at earlier time-points. Consequently, a 5-day treatment may have been too long to capture the more acute EMT-like response and the concurrent upregulation of *MMP7*. To investigate this, a follow-up experiment was conducted with A549 cells treated with TGF-β alone in a 3-day time-course study. Additionally, FC and StemXvivo conditions were included as well. Note that the 10, 3 and 0.3 ng/ml TGF-β conditions were the same concentration as the TGF-β present in 1X, 0.3X and 0.1X FC. A549 cell lysates were analysed for the same markers as before, with the addition of αVβ6 integrin (measured as *ITGB6*, the mRNA encoding for the β6-subunit).

The *MMP7* qPCR data revealed a similar pattern of downregulation as seen in the previous experiment (Figure 12). Compared to vehicle control, expression levels decreased in a time-dependent manner across all conditions. Compared to their respective vehicle controls, StemXVivo treatment reduced *MMP7* expression by approximately 65% within 24 hours, while FC-treatment downregulation *MMP7* only at 48 and 72h post-treatment. At higher concentrations, TGF-β (10, 3, and 1 ng/mL) induced *MMP7* downregulation comparable to StemXVivo, whereas no reduction was seen for the lower TGF-β doses (0.3 and 0.1 ng/mL). Notably, TGF-β alone induced greater *MMP7* downregulation compared to the FC, which also includes TGF-β. A549 cells treated with StemXVivo, FC and TGF-β (10 and 3 ng/ml) showed respectively ~7-fold, ~2.5-fold and ~6-fold increase in *ITGB6* gene expression at 72h post-treatment (Figure 13).

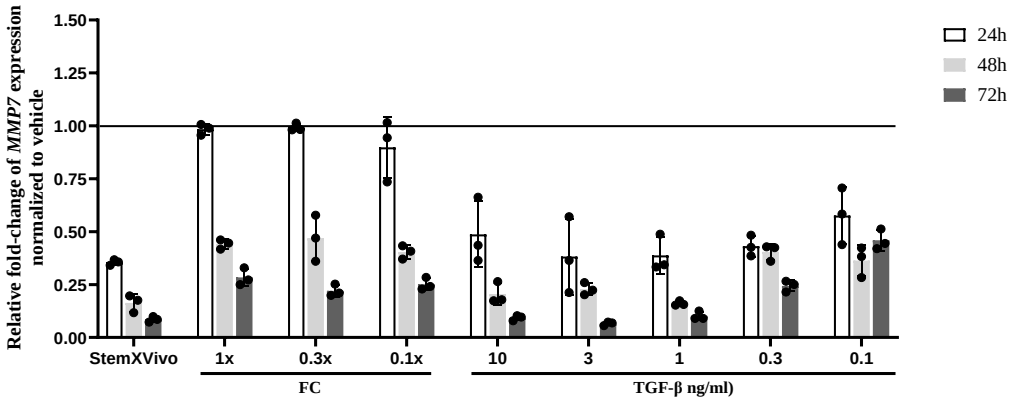

Figure 12. Gene expression data showing fold-changes MMP7 mRNA expression relative to vehicle (PBS and control cocktail), evaluated 24h, 48 and 72h post-treatment with StemXVivo, fibrotic cocktail (FC) and TGF-β alone. MMP7 expression was downregulated in a time-dependent manner. TGF-β alone induced a higher downregulation of MMP7 compared to the fibrotic cocktail, indicating that it plays an important role in the observed downregulation of MMP7.

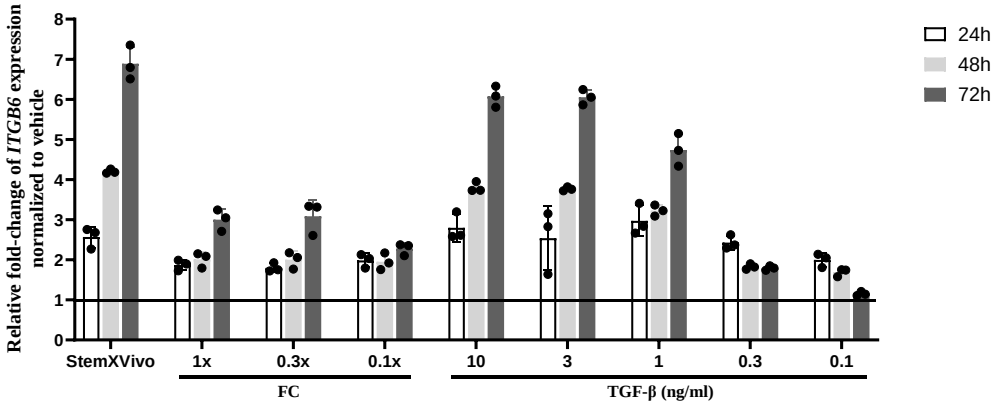

Figure 13. Gene expression data showing relative n-fold induction of ITGB6 compared to vehicle (PBS and control cocktail), evaluated 24h, 48 and 72h post-treatment with StemXVivo, fibrotic cocktail (FC) and TGF-β alone. ITGB6 gene expression relative to vehicle control was increased by approximately 7-fold 72h post-treatment with StemXVivo, 3-fold 72h post-treatment with FC (1X & 0.3X) and 6-fold 72h post-treatment with TGF-β (10 ng/ml & 3 ng/ml).

Similarly, *VIM* expression was upregulated in response to FC and StemXVivo compared to vehicle control (Figure 14). *VIM* was however upregulated to a lesser degree in response to TGF-β alone. *KRT17* on the other hand, was only upregulated in cells treated with StemXVivo and TGF-β. The expression peaked 24h post-treatment across the specified conditions and returned gradually to baseline levels in the later time-points. Notably, the StemXVivo treatment induced higher upregulation of *ACTA2* compared to the other treatments. The expression level increased in a time-dependant manner, with the highest expression, approximately 1.8-fold higher compared to vehicle control (PBS), observed 72h post-treatment with StemXVivo. *SFTP-C* expression was markedly reduced across all conditions, notably so in response to treatment with the fibrotic cocktail. The overall data indicated that the A549 cells were pushed towards a more EMT-like phenotype, albeit with significant downregulation of *MMP7*.

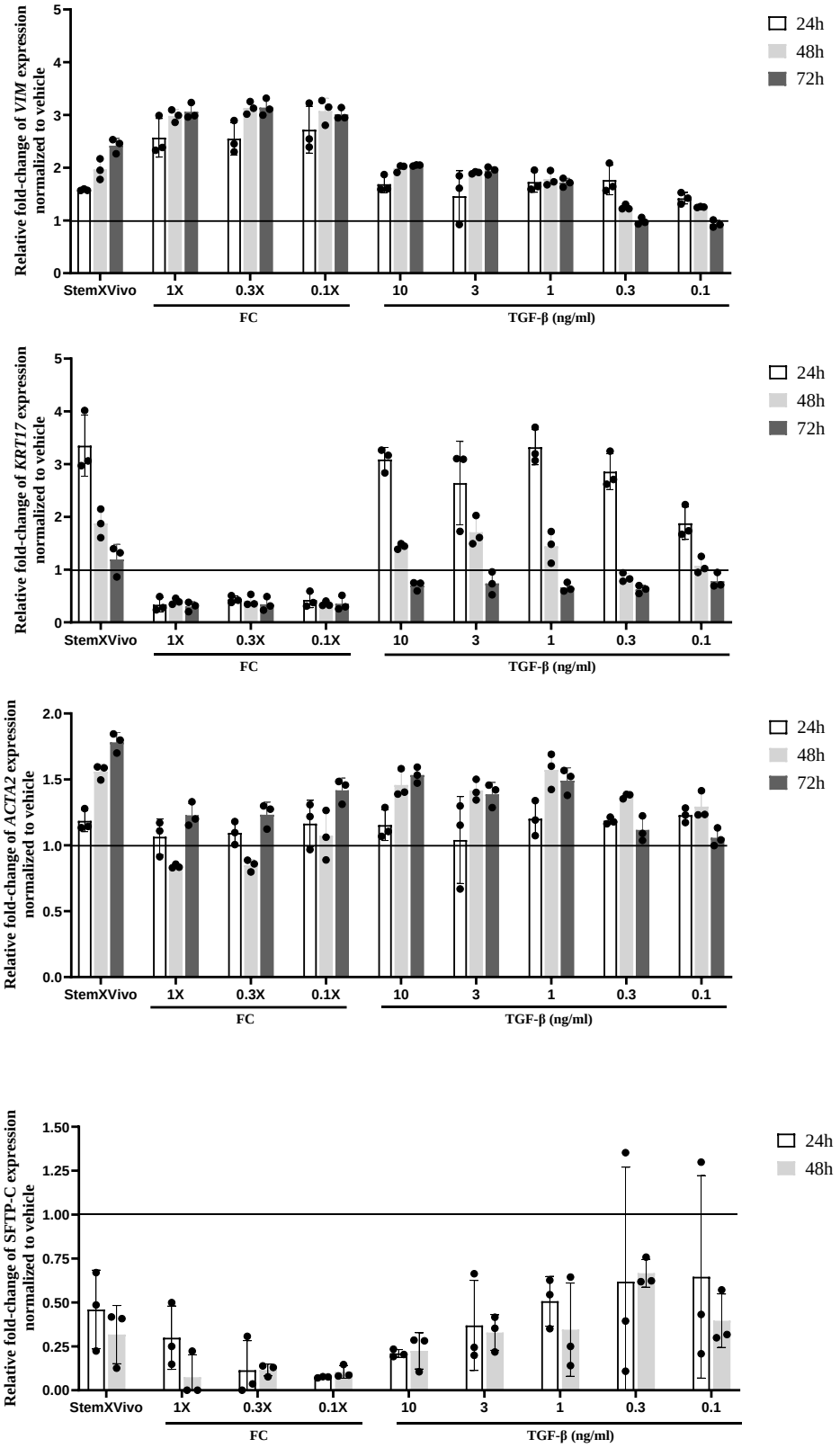

Figure 14. Gene expression data showing fold-changes VIM, KRT17, ACTA2 and SFTP-C mRNA expression relative to vehicle (PBS and control cocktail), evaluated 24h, 48 and 72h post-treatment with StemXVivo and fibrotic cocktail (FC). The 72h time-point for SFTP-C was not included due to technical problems with qPCR data generation. The EMT markers confirm the transition of A549 cells to a more mesenchymal-like phenotype, with the StemXVivo producing the most pronounced EMT response.

Since treatment with the common EMT/fibrosis inducing compounds induced a significant downregulation of *MMP7* at both mRNA and protein level, we decided to test an additional profibrotic mediator, being osteopontin. Osteopontin was confirmed to induce an upregulation of *MMP7* in A549 in a study by Pardo et al. (2005). Consequently, we proceeded to evaluate this in a time-course study, measuring EMT-like responses and *MMP7* gene expression levels 24 and 48h post-treatment with osteopontin and StemXVivo as a positive control. A549 cell lysates were analysed for the expression of *MMP7*, *VIM*, *SFTP-C* and *ACTA2*.

MMP7 gene expression remained unchanged across all osteopontin concentrations and time-points (Figure 15). Osteopontin did not induce expression of any of the analyzed EMT markers, but we did see a 40% downregulation of *SFTP-C* gene expression with 3 µg/mL at 48h post-treatment as compared to vehicle control. *MMP7* was downregulated 30% and 66% in each time-point respectively for cells treated with StemXvivo versus vehicle control. While the EMT response and *MMP7* downregulation was similar to previous experiments with the StemXVivo treatment, osteopontin did not affect any of the markers. Altogether, treatment with StemXVivo, FC and TGF-β increased aberrant basaloid markers in A549 cells, but did not lead to increased *MMP7* expression whereas treatment with osteopontin did not have any effect on EMT markers or *MMP7* expression.

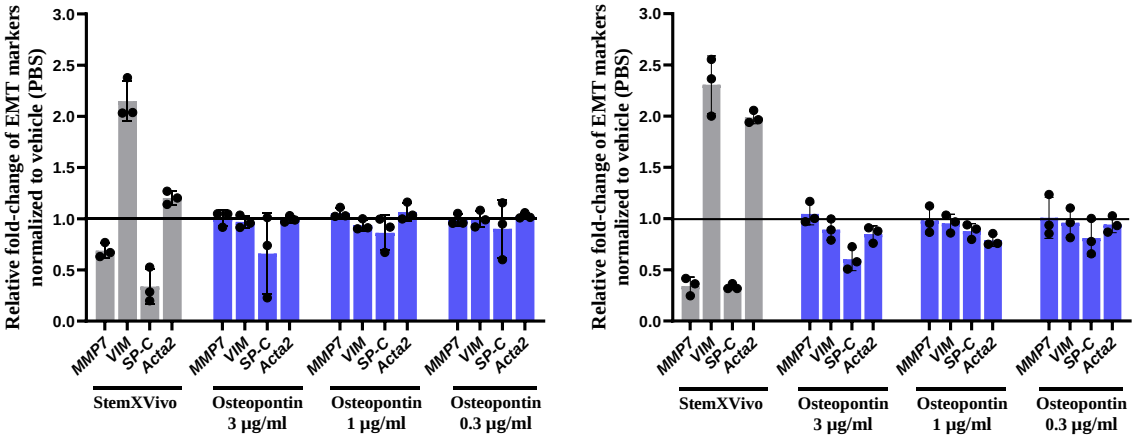

Figure 15. Gene expression data showing mRNA expression of MMP7, VIM, SFTP-C and ACTA2 relative to vehicle (PBS), evaluated 24h (left) 48h (right) post-treatment with 3, 1 and 0.3 µg/ml osteopontin. StemXVivo treatments were included as a positive control for the EMT response. No change in EMT markers and MMP7 gene expression was seen in cells treated with osteopontin.

3. Delivery of αVβ6-targeted siRNA and modelling fibrosis induced epithelial damage in human alveolar organoids

While cell lines such as 16HBE and A549 offer advantages such as ease of use, relatively low cost and high throughput, they do not fully capture the complexity of real biological systems and are thus limited in translational applications. Next in line of *in vitro* models are induced pluripotent stem cell-derived 3D human alveolar organoids. The organoids are grown on Matrigel, a mixture of laminin, collagen and entactin, as well as various growth factors and signalling molecules required for proper differentiation into AT2 cells. Alveolar organoids have proven to successfully recapitulate the aberrant basaloid phenotype in response to fibrotic cocktail and important aspects of IPF pathophysiology (Ptasinski, et al., 2023). In comparison, both 16HBE and A549 cell lines are immortalized and can differ significantly in some genetic expression patterns compared to alveolar epithelial cells obtained from naïve sources. The weak *MMP7* response in 16HBE cells and the significant downregulation in A549 cells from previous experiments indicated a clear deviation from the expected EMT-like induction pattern. Hence, we shifted our focus towards the human alveolar organoids to validate the delivery of SM-conjugated siRNA and further develop a biological effect assay used for delivery of a functional cargo (MMP7).

3.1 Naked and SM-conjugated siRNA achieved comparable *PPIB* KD in alveolar organoids

Naked and SM-conjugated PPIB siRNA delivery was evaluated in human alveolar type 2 organoids derived from pluripotent stem cells in a 72h dose-response study. Positive controls were included by transfecting the organoids with PPIB siRNA using Lipofectamine RNAiMAX reagent. Cell lysates were analysed for the *PPIB* gene expression using qPCR. Ubiquitin C (*UBC*) and ribosomal protein L13a (*RPL13a*) genes were used as housekeeping gene controls. Naked and SM-conjugated PPIB siRNA both induced respectively ~30 % and 14% KD at 10 and 1 µM compared to vehicle control (Figure 16). RNAiMAX transfection of both naked and SM-conjugated siRNA induced an average KD of only 10% and 36% respectively as compared to vehicle control. There is overall no clear differentiation between naked and SM-conjugated PPIB siRNA in the alveolar organoids. The KD is modest across all conditions as compared to A549, transfection samples included. However, a potential trend of dose-response for the SM-conjugated siRNA was observed.

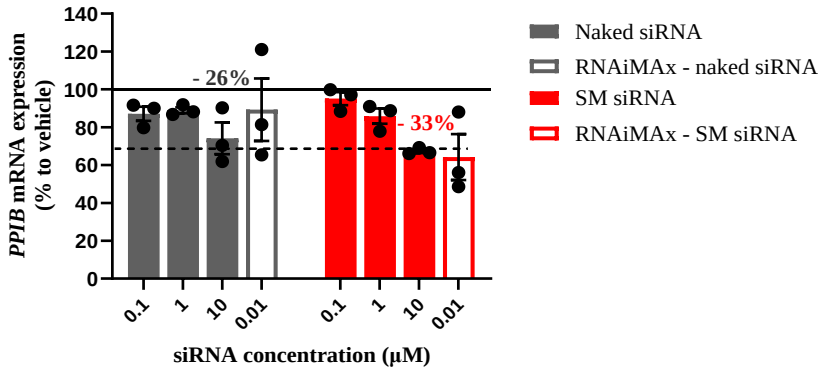

Figure 16. Gene expression data showing the dose-response KD 72h post-treatment with 0.1, 1 and 10 µM naked and SM-conjugated PPIB siRNA. While both siRNA performed similarly across all conditions, SM-conjugated siRNA induced a potentially dose-dependent KD, which may be captured more clearly in a later time-point

3.2 Retention of siRNA on Matrigel surface significantly limits uptake by alveolar organoids

To investigate if the overall modest KD was due to inefficient siRNA delivery into organoids, Uptake of naked and SM-conjugated siRNA was also evaluated in alveolar organoids 18h post-treatment. Organoids were treated with 1 µM of Alexa Fluor 647 labelled naked and SM-conjugated PPIB siRNA,

as well as RNAiMAX transfected 0.01 µM siRNA (naked and SM-conjugated). Organoids were stained with nuclear counterstain post fixation. siRNA uptake is illustrated for each condition (one well per condition) where two images are provided from two different focal planes (Figures 17 and 18). Due to the Matrigel-coating in the bottom of the wells forming a rather concave than flat surface, the "bottom view" is provided to highlight the surface in middle of the wells and as well as a "top view" to capture the organoids near the edges of the wells. The majority of siRNA were stuck on the surface of the Matrigel. This was evident by the increasing diameter of the siRNA signal (red) following the concave shape of the Matrigel-coating, as the focal point was shifted from the bottom view to the top view. We were unable to quantify the uptake, as most of the siRNA was retained to the Matrigel with minimal uptake in organoids across all conditions. Overall, there was no observed difference in uptake observed between naked and SM-conjugated siRNA and delivery as such was not deemed successful.

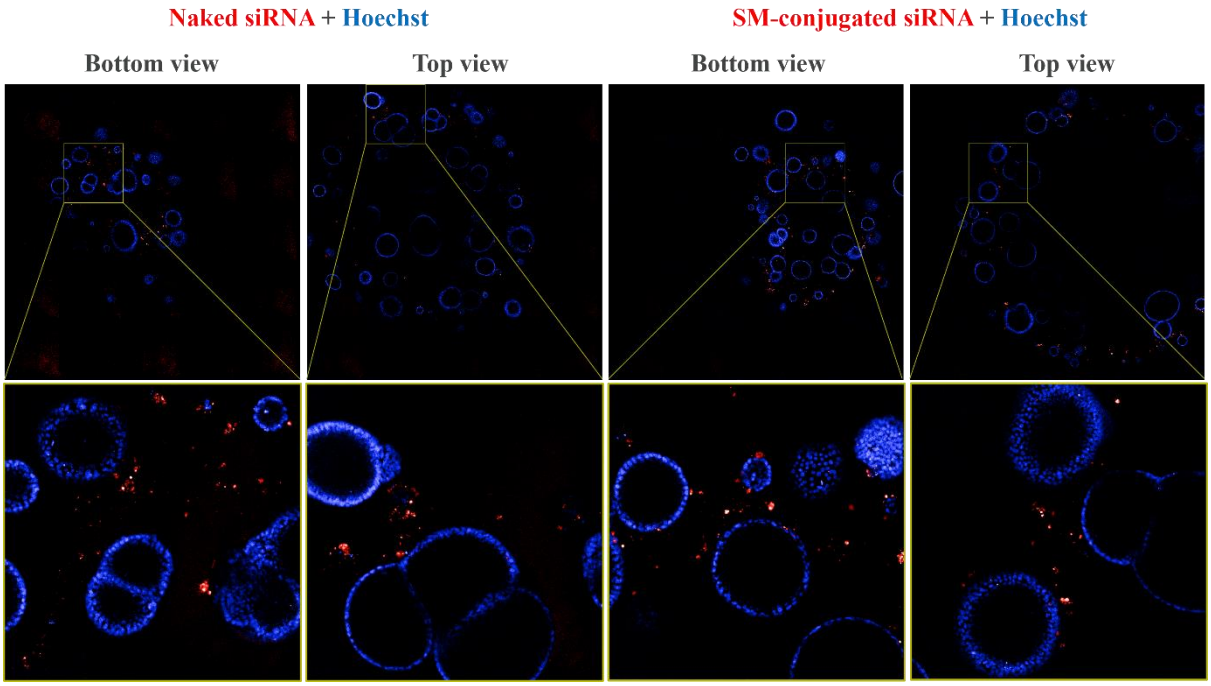

Figure 17. Imaging results of the uptake of 1µM naked and SM-conjugated siRNA (red) in alveolar organoids 18h post-treatment. Organoids were stained with Hoechst nuclear counterstain (blue) to visualize the organoids. Each condition is represented by two images from two different focal points: one representing the middle portion of the Matrigel (bottom view) and one representing the edges of the Matrigel (top view). The bottom panels represent higher magnification images, showing a clear retention of both naked and SM-conjugated siRNA on the Matrigel and minimal uptake by the alveolar organoids.

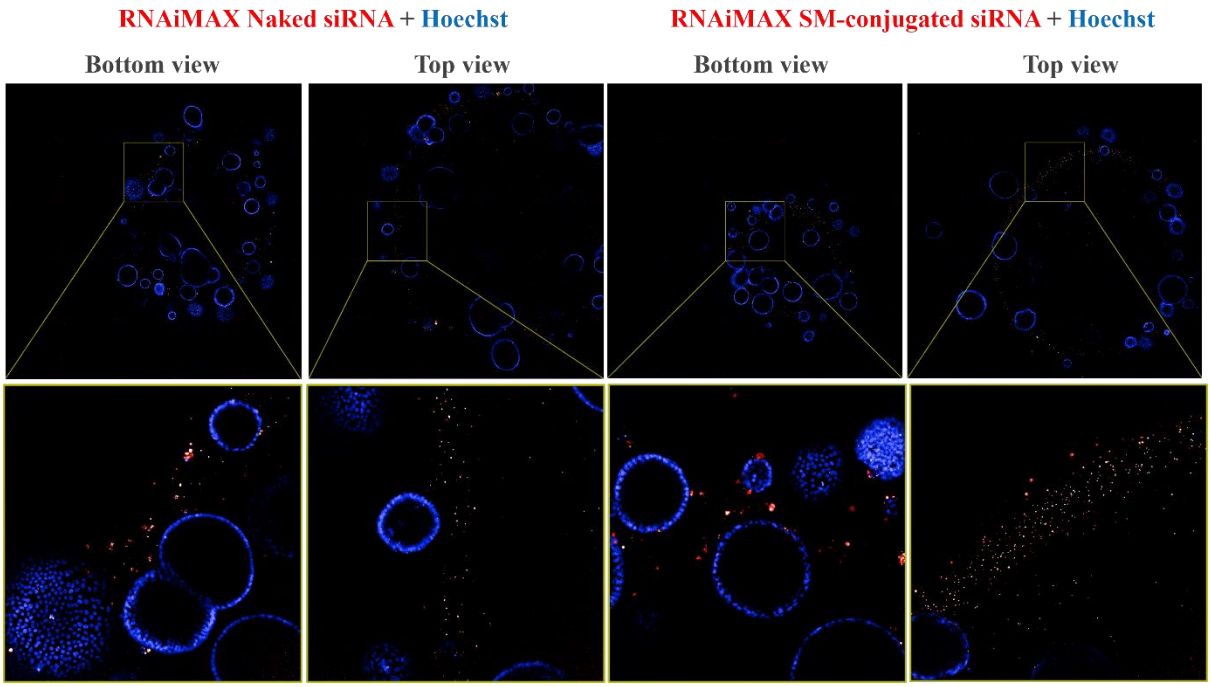

Figure 18. Imaging results of the uptake of 0.01 µM RNAiMAX transfected naked and SM-conjugated siRNA (red) in alveolar organoids 18h post-treatment. Organoids were stained with Hoechst nuclear counterstain (blue) to visualize the organoids. Each condition is represented by two images from two different focal points: one representing the middle portion of the Matrigel (bottom view) and one representing the edges of the Matrigel (top view). The bottom panels represent higher magnification images, showing a clear retention of both naked and SM-conjugated siRNA on the Matrigel and minimal uptake by the alveolar organoids.

3.3 Alveolar organoids treated with fibrotic cocktail show elevated MMP7 mRNA and protein expression

Aberrant epithelial reprogramming has been observed in alveolar organoids treated with a standard fibrotic cocktail in previous publications (Ptasinski, et al., 2023). However, *MMP7* and *αVβ6* expression in this system had not been previously analysed. To this end, we evaluated the EMT response and the concurrent *MMP7* expression in a 72h time-point experiment. Alveolar organoids were treated with 0.6X, 0.3X and 0.15X dilutions of the 'standard' fibrotic cocktail component concentrations. Cell lysates were analysed for *MMP7*, *αVβ6*, *VIM*, *KRT17* and *SFTP-C* expression, with *UBC* and *RPL13a* used as housekeeping control genes. Additionally, total MMP7 protein concentration was measured in the supernatants via ELISA.

MMP7 gene expression was elevated by approximately 8.6-, 7.5- and 6.5-fold in response to 72h treatment with fibrotic cocktail (0.6X, 0.3X and 0.15X respectively) as compared to vehicle control (control cocktail) (Figure 19). A similar trend was observed in the total MMP7 protein concentration in supernatants (Figure 20). Total MMP7 concentration was increased by 5.8-, 5.2- and 4.2-fold (0.6X, 0.3X and 0.15X respectively), as compared to vehicle control. Notably, the fibrotic cocktail induced on average a 15-, 11.8- and 6.20-fold upregulation of *ITGB-6* mRNA (0.6X, 0.3X and 0.15X respectively), compared to vehicle control. Together with the upregulation of *VIM*, *KRT17* and downregulation of *SFTP-C*, the fibrotic cocktail induced a clear EMT-like response.

We also evaluated *MMP7* gene expression in alveolar organoids treated with 0.6X fibrotic cocktail in a 48h time-point study, performed independently. *MMP7* was upregulated by approximately 13-14-fold compared to vehicle (Figure 21), further confirming that *MMP7* expression is significantly increased in response to fibrotic vs control cocktails.

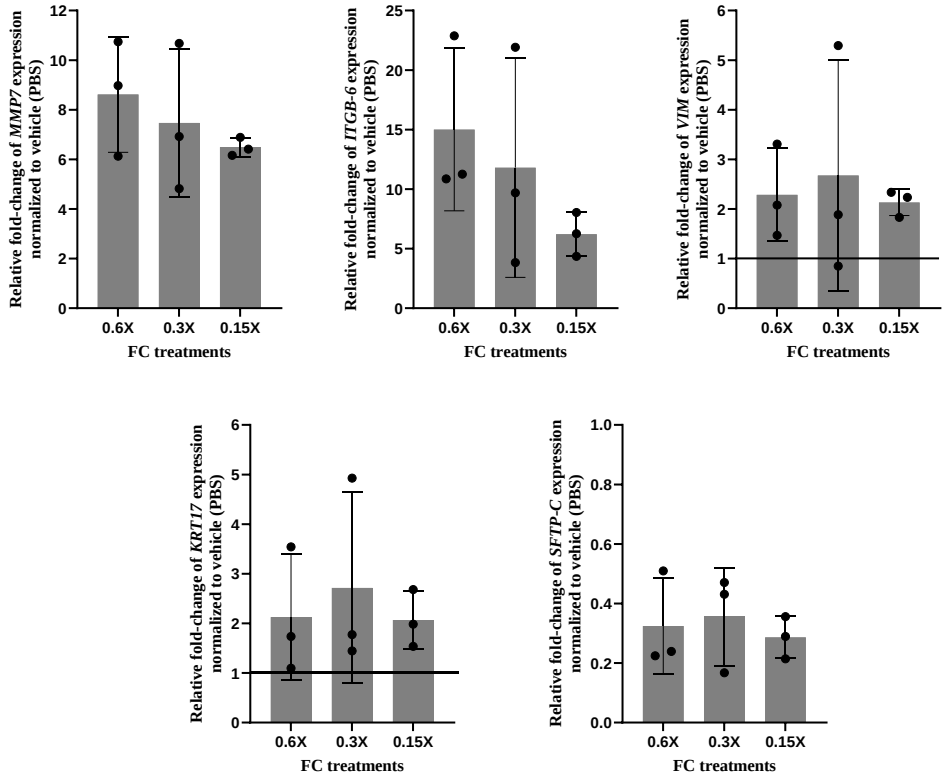

Figure 19. Gene expression data showing the mRNA expression of MMP7, αVβ6, VIM, KRT17 and SFTP-C relative to vehicle control (control cocktail), evaluated 72h post-treatment with 0.6X, 0.3X and 0.15X dilutions of the fibrotic cocktail. Highly elevated MMP7, VIM, KRT17 and significant downregulation of SFTP-C indicates a strong EMT response even at lower doses of fibrotic cocktail.

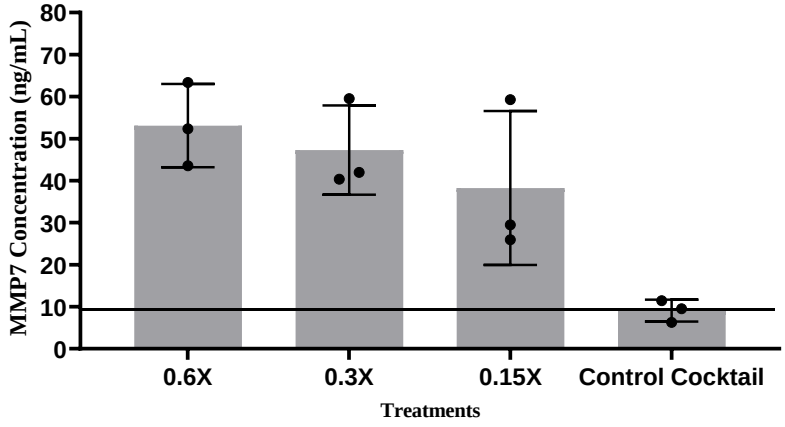

Figure 20. MMP7 concentration measured via ELISA in supernatants collected from alveolar organoids 72h post-treatment with 0.6X, 0.3X and 0.15X dilutions of the fibrotic cocktail. Significant elevation in secreted MMP7 was observed across all conditions, as compared to control cocktail (PBS).

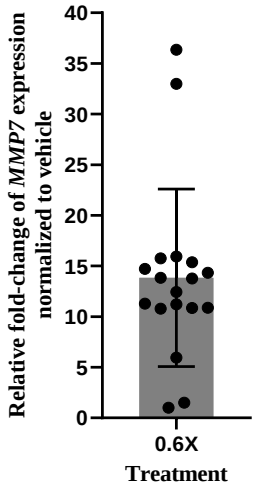

Figure 21. Gene expression data showing the mRNA expression of MMP7 relative to vehicle control (control cocktail), evaluated 48h post-treatment with 0.6X dilution of fibrotic cocktail. cDNA was acquired from an independent project where cell work, RNA extraction and cDNA synthesis were performed by a peer. 0.6X FC induced an average MMP7 mRNA upregulation of 1300-1400% as compared to vehicle control.

Discussion

In this thesis, three different *in vitro* models were evaluated as potential biological effect assay for the delivery of an αVβ6-ligand conjugated *MMP7* siRNA. The 16HBE cell line marked the starting line of this thesis, with siRNA uptake and delivery assays already successfully established. Based on the research paper by Gill et al. (2016), the authors describe a role for MMP7 in the release of IL-8 from injured epithelial cells. We therefore theorized that by inducing an inflammatory response in the 16HBE cell line, the release of the chemoattractant IL-8 into the supernatant could potentially be mediated by MMP7. Cells were treated with lipopolysaccharide (LPS), a potent inducer of acute inflammation. LPS is the major component of the outer layer of gram-negative bacteria cell wall and induces the host's innate immunity primarily by binding to the pattern recognition receptor TLR4. Although the TLR4 receptors are mainly expressed by immune cells like macrophages and monocytes, the expression extends to a lesser degree to include epithelial cells as well (Crame, et al., 2021) (Nighot, et al., 2017). Therefore, we expected to observe an inflammatory response similar to an injured state of epithelial cells, including the upregulation of MMP7. However, upon analysing the cell lysates for the expression of *IL6*, *IL8* and *MMP7* mRNA, it was clear that despite the initial spike in *IL6* and *IL8* expression at early time-points and higher LPS concentrations, no clear induction of *MMP7* expression was observed. From a biological standpoint, it is highly likely that the weak inflammatory response was due to the low expression of TLR4 receptors in epithelial cells and cell lines in general. Taken together, the overall response to LPS in 16HBE cells was deemed weak, being the reason that MMP7 expression was not significantly induced. One limitation of this experiment was the lack of MMP7 protein measurement, as the levels of secreted MMP7 does not always correlate with the mRNA expression. Additional improvements to the experiment setup may include optimization of the LPS doses and time-points to further improve the resolution of the inflammation response.

16HBE cells were also stimulated with TNF-α, a potent cytokine that is secreted by immune cells in response to inflammation inducing agents, such as LPS. TNF-α binds to the TNFR1 and TNFR2 receptors on the surface of epithelial cells, mediating various inflammatory pathways as a part of the epithelial-immune cell crosstalk. The expression of TNFR1 and TNFR2 in epithelial cells are higher than TLR4, thus rendering the cells more sensitive to TNF-α than LPS. To that end, TNF-α was chosen as a downstream surrogate for LPS. However, 16HBE cells displayed minimal increase in *MMP7* mRNA expression 6h post-treatment with TNF-α, with the exception being the 33.3, 100 and 300 ng/ml

concentrations. The expression however was increased somewhat, where an acute inflammation response (as seen with IL-6 and IL-8) was seen followed by a delayed increase in MMP7 shortly thereafter. Taken together, the upregulation of MMP7 expression in response to treatment with the proinflammatory compounds LPS and TNF-α was not deemed sufficiently high to be of significance. As a continuation of this experiment, we suggest utilizing MMP7-negative (knock-out) 16HBE cells as a negative control to further increase the power of the results. It is also important to note that 16HBE is a cell line derived from airway bronchial epithelial cells. Consequently, the expression of TNFR1 and TNFR2 may be more restricted to alveolar epithelial cells, explaining the weak response to TNF-α in the 16HBE cell line. To conclude, due to the weak MMP7 response and difference in origin and function compared to that of alveolar epithelial cells, we decided to evaluate other cell systems.

The lung adenocarcinoma cell line A549 was evaluated for productive delivery of αVβ6 receptor-mediated siRNA delivery. Delivery and uptake of naked and SM-conjugated siRNA was evaluated using the tool siRNA targeting the housekeeping gene PPIB (Figures 7 and 8). The SM-conjugated siRNA induced over 50% KD at 10 μM 48h and 72h post-treatment, compared to vehicle control. In addition, the SM-conjugated siRNA at 1 μM in both time-points induced similar KD to that of 10 μM naked siRNA, indicating a 10X shift in therapeutic window. This translates into lower required dose of SM-conjugated siRNA to reach the same KD window. The lipofectamine transfected naked and SM-conjugated siRNA both achieved more than 90% KD compared to vehicle, indicating that when the uptake bottleneck is removed through highly efficient carrier molecules, the designed sequence is highly effective at knocking down the target mRNA, further validating the target engagement. Moreover, this result suggests that the SM-ligand likely does not interfere with the RISC loading of the siRNA and does not affect the gene silencing similar to the unconjugated siRNA. The difference in KD efficiency was further supported by the observation of 4-fold higher MFI signal of SM-siRNA compared to naked siRNA. Seeing the clear difference in the αVβ6 surface expression compared to 16HBE cells in Figure 6, the result was contrary to what was believed at first. It can be concluded that despite the significantly lower surface expression of αVβ6 by A549 cells, the KD efficiency was equal if not better than what was seen in 16HBE cells (data not shown). It seems that the surface expression of αVβ6 receptors do not solely determine the efficiency of the siRNA uptake/KD. Consequently, the uptake and internalization pathways of the A549 cell line may be different to that of the 16HBE cells, which needs further investigation. We speculate that this could be due but not limited to higher rate of αVβ6-receptor recycling or better endosomal escape efficiency in the A549 cell line. Nevertheless, the current research on uptake, internalization, receptor recycling and comparative studies between the established cell lines are lacking in this area.

As for the fibrosis assay, A549 cells have been utilized in a number of studies for establishing mechanisms of induced lung injury and EMT-related pathology in diseases such as cancer and lung fibrosis (Kasai et al., 2005) (Chen, et al., 2016) (Tirino, et al., 2013) (Ou, et al., 2020). To this end, we tested the effect of various profibrotic mediators on MMP7 secretion by A549 cells. As seen in our initial testing (Figure 10), the MMP7 mRNA expression was significantly downregulated in response to the 5-day treatment with StemXVivo and fibrotic cocktail. The loss of SFTP-C mRNA expression and upregulation of VIM, KRT17 and ACTA2 however indeed indicated that the A549 cells had assumed a more mesenchymal phenotype. MMP7 concentration in the supernatants also demonstrated significant reduction in protein levels, as seen in Figure 11. Notably, the MMP7 protein concentration in supernatant seen in the negative control groups confirmed the high basal expression, similar to what has been shown in the literature (Jaffar, et al., 2022). Initially, we expected to see a clear upregulation of MMP7 in response to the fibrotic cocktail, StemXVivo or osteopontin. Specifically, Pardo et al. (2005) demonstrated that MMP7 mRNA level was highly elevated (6-fold changes in gene copy number) in A549 cells treated with osteopontin. However, we were unable to replicate this result, as seen by the lack of MMP7 mRNA induction.

We hypothesized that perhaps the TGF-β in StemXVivo and fibrotic cocktail, the main driver of an EMT-like process in A549 cells, contributed to this downregulation, and that the MMP7 expression may have peaked at earlier time-points. For that reason, and to investigate the effect of TGF-β alone on the cells, we proceeded to perform a time-course experiment and measured the gene expression 24h, 48h and 72h post-treatment. Similar to the 5-day treatment, the *MMP7* expression was noticeably downregulated, counter to our expectations. The most noticeable downregulation was again observed in cells treated with StemXVivo, which also was the treatment that displayed the most significant induction of the mesenchymal markers. The decrease in *MMP7* became more prominent as the mesenchymal markers *VIM*, *ACTA2* and *KRT17* were upregulated (and SFTP-C was downregulated) during later time-points, indicating a reverse relationship between the MMP7 gene expression and the EMT markers. Cells treated with the fibrotic cocktail displayed a similar pattern, albeit to a lesser degree, with the *MMP7* expression being downregulated in a time-dependant but concentration-independent manner. TGF-β alone induced an *MMP7* downregulation to lesser extent as compared to the fibrotic cocktail, which could indicate that the other components of the fibrotic cocktail counteracted the downregulation to some extent. In addition, mRNA expression of *ITGB6* was significantly upregulated in a clear time dependent manner, most notably in cells treated with StemXVivo and TGF-β. Comparing the fibrotic cocktail to TGF-β by itself, it seems that the *ITGB6* expression was not as highly upregulated. It is unclear however whether this is due to the same reason as the MMP7 downregulation trend mentioned earlier. Overall, the data suggest that the A549 cell line undergoes an EMT-like process, however the MMP7 response deviated from the expected pattern. Our hypothesis is that firstly, the A549 cells are derived from cancer cells and while they exhibit an aberrant basaloid-like phenotype and partial EMT that reflects a fibrotic state, they may significantly deviate in other pathways (Li, et al., 2024). EMT in cancer differs from what is observed in IPF, thus the degree of EMT and cell origin may dictate what markers are expressed. Secondly, the mechanisms behind the upregulation of MMP7 in lungs of IPF patients is currently not fully understood. Richards et al. (2012) suggested that single nucleotide polymorphisms of the MMP7 promoter created a novel binding site for the FOXA2 transcription factor, which regulates the fate of epithelial cells, and is also involved in the sonic hedgehog pathways (Wan, et al., 2005) (Paranjapye, Mutolo, Ebron, Leir, & Harris, 2020). The authors explain in their findings that the colocalization of FOXA2 and MMP7 mRNA in the cytoplasm was a driving factor of MMP7 upregulation. In another study, Zhang et al. (2011) demonstrated that A549 cells treated with TGF-β1 induced downregulation of FOXA2 through the TGF-β1/SMAD3 signal transduction pathay, which may explain the downregulation of MMP7 in our experiments. However, it is worth noting that since a drastic downregulation of *MMP7* was observed after merely 24h (Figure 12), TGF-β may have impacted *MMP7* through a more direct pathway. To conclude, while the A549 cell line is a suitable system for αVβ6-targeted siRNA delivery per se, we deemed it not as suitable for the envisioned biological effect assay. Therefore, we utilized lung alveolar organoids that were derived from induced pluripotent stem cells (iPSC), to adress the aformentioned limitations experienced with the A549 cells.

Delivery and uptake of siRNA proved to be a limitation of this system. The naked and SM-conjugated siRNA performed similarly in terms of KD potency 72h post-treatment. However, while the KD percentage at maximum dose of naked and SM-conjugated siRNA were similar, the SM-conjugated siRNA tended to follow a dose-dependent pattern. This could imply that additional later time-points may yield a clearer KD window. It is also important to note the poor KD of the RNAiMAX siRNA transfection. siRNA transfections are positive controls used to validate target engagement in *in vitro* siRNA delivery experiments. It is unlikely that the siRNA sequence itself failed to induce a KD, as the target engagement has been validated in several *in vitro* and *in vivo* models (data not shown) and the SM-ligand does not interfere with RISC loading as demonstrated with A549 cells. Various other transfection kits were tested and Lipofectamine 2000 Transfection Reagent performed best (data not shown) and is recommended in future experiments. Uptake of naked and SM-conjugated siRNA was also evaluated in the alveolar organoids. Interestingly, the pattern of the siRNA signal (Figures 17 and

18) resembled that of a circular halo which followed the concave shape of the Matrigel. Since the siRNA is negatively charged, it was possible that most of the siRNA was retained on the positively charged Matrigel (which contains laminin and collagen that are polar). This retention may explain why there was no clear difference in KD between naked and SM-conjugated siRNA, as both were equally trapped on the Matrigel gel surface. The composition of Matrigel is highly complex and poorly defined, making it challenging to determine the exact mechanism of siRNA retention. Kozlowski et al. (2021) discussed several alternatives to Matrigel, such as decellularized ECM derived from tissues, synthethic hydrogels and gels formed from recombinant proteins. It remains to be seen whether these alternatives alleviate the siRNA delivery challenge mentioned above while preserving the appropriate conditions that allow alveolosphere growth and survival. In conclusion, repeats of the KD experiment is required with the addition of later time-points and the siRNA transfection needs to be optimized with respect to titration and kits used to ensure a proper positive control.

On the other hand, we demonstrated that the organoids expressed a clear MMP7 upregulation after treatment with the fibrotic cocktail as compared to vehicle control, even at the lowest dose. The upregulation of *ITGb-6*, *VIM*, *KRT17* and downregulation of *SFTP-C* markers indicated a mesenchymal-like phenotype across all fibrotic cocktail concentrations. Alveolar organoids have a higher biological complexity compared to cell lines and have proven to be suitable for developing biological effect assay for MMP7 targeted siRNA in a fibrosis-related context, as demonstrated here. However, the delivery of the siRNA remains a challenge as the siRNA is captured on the surface of the Matrigel in the cultures, impeding the uptake and hence KD efficiency. Additionally, it needs to be considered that alveolar organoids require one month to mature (Jacob, et al., 2019), therefore limiting experimental throughput.

Conclusion & Prospects

siRNA therapeutics have the capacity to target disease-related gene products that are otherwise pharmacologically difficult to target by conventional small molecules. By expanding the druggable space, siRNA therapeutics offer new possibilities to treat rare diseases with unmet needs, such as IPF and other lung fibrotic diseases. Despite technological advances, efficient delivery of siRNA to the tissue/cell type of interest remains a major limitation. In this thesis, we explored an αVβ6-mimetic ligand conjugation for targeted delivery of siRNA in epithelial cells as a potential solution to overcome this limitation. Here we aimed to deliver a disease-related, functional siRNA cargo and to assess its efficacy, using three distinct and well-established cell systems to develop an *in vitro* biological effect assay. Using a small molecule ligand-conjugated siRNA designed to target *MMP7* as a potential treatment of IPF, we aimed to develop an assay accordingly that recapitulated key aspects of pulmonary fibrosis.

Each system has its strength and weakness. We have shown that the A549 cell platform can be used to evaluate the uptake and delivery of αVβ6-ligand conjugated siRNAs and can acquire an aberrant basaloid phenotype in response to a profibrotic stimulus. This system however did not show upregulation of MMP7, which limits its use as a biological effect assay. On the other hand, alveolar organoids derived from induced pluripotent stem cells, recapitulated the aberrant basaloid expression pattern and the concurrent MMP7 upregulation when treated with a fibrotic cocktail. However, uptake and delivery of the siRNA remains a challenge due to the complexity of this system. We were unable to draw conclusions about the potency of the siRNA. siRNA dosage, transfection and staining protocols needs more optimization.

Although the alveolar organoids offer clear advantages over cell lines in terms of biology, they are limited in terms of throughput, ease of use and availability. To that end, future experiments can still include the A549 cell line, using their constitutive MMP7 secretion to an advantage. Alternative methods to analyse the biological effects of MMP7-targeted siRNA such as scratch-wound and migration assays can be useful. MMP7-dependent migration and proliferation can be studied in these

assays, and siRNA-induced KD of this gene can provide valuable insight of the therapeutic potential of this oligonucleotide molecule. Alternative systems include precision-cut lung slices (PCLS) and whole lung explants as the logical next step from alveolar organoids. Although these tools are not easily scalable, they do have the potential to be more translatable. They can be derived from human diseased tissue or from animal models and kept immersed in culture medium (Sacchi, Bansal, & Rouwkema, 2020). This could potentially mitigate the delivery problem due to Matrigel siRNA retention. However, delivery may still be limited due to the siRNA needing to penetrate the PCLS tissue layers to reach the desired therapeutic window.

Materials & Methods

Cell lines

16HBE was cultured in high glucose Gibco DMEM (1X) + GlutaMAX (catalogue number 31966-021), supplemented with 10% heat inactivated FBS (Gibco, catalogue number A5256801) and 1% PEST (Gibco, catalogue number 15140122).
A549 was cultured in Gibco DMEM/F-12 (1:1) (1X) + GlutaMAX medium (catalogue number 31331-028), supplemented with 10% heat inactivated FBS and 1% PEST.
Human lung alveolar organoids derived and cultured according to the protocol by Jacob et al. (2019)

siRNA transfection protocol

For siRNA transfection, the Lipofectamine™ RNAiMAX Transfection Reagent kit was used (ThermoFisher Scientific, catalogue number 13778030). siRNA was diluted from 10 µM to 0.2 µM using Opti-MEM Reduced Serum Medium (Gibco, catalogue number 31985062). Lipofectamine master mix was prepared by mixing 1.5 µl Lipofectamine RNAiMAX with 25 µl Opti-MEM medium. The diluted 0.2 µM siRNA was then mixed the lipofectamine master mix in equal volumes. The mixture is incubated for 5 minutes at room temperature and 10 µl was added to the corresponding wells

Compounds list used in biological effect assay

Lipopolysaccharide (LPS) from Escherichia coli, strain O127:B8 - Sigma-Aldrich, catalogue number L4516
Recombinant Human TNF-a - R&D Systems, catalogue number 10291-TA-020
Recombinant Human TGF-β - R&D Systems, catalogue number 240-B-010
Recombinant Human PDGF-AB - Gibco, catalogue number PHG0134
1-Oleoyl Lysophosphatidic Acid (LPA) - Cayman Chemical, catalogue number 62215
StemXVivo EMT Inducing Media Supplement - R&D Systems, catalogue number CCM017
Recombinant Human Osteopontin - R&D Systems, catalogue number 1433-OP-050/CF
Fibrotic cocktail (FC) components, see the Table 1 and 2.

Table 1. List of compounds in the fibrotic cocktail and their stock concentrations. All subsequent dilutions used in the experiments were derived from the 10X working concentration.

FC Components	Stock concentration	10X concentration	Volume needed for 400 µl 10X FC
TGF-β	20000 ng/mL	100 ng/mL	2 µl
TNF-α	100000 ng/mL	200 ng/mL	0.8 µl
PDGF-AB	100000 ng/mL	200 ng/mL	0.8 µl
LPA	23000 µM	100 µM	1.74 µl

Table 2. List of compounds in the control cocktail, containing the vehicle compounds and their stock concentrations. Similar to the fibrotic cocktail, all subsequent dilutions used in the experiments were derived from the 10X working concentration.

CC Components	Stock concentration	10X concentration	Volume needed for 400 µl 10X FC
4 mM HCl + 0.1% BSA	20000 ng/mL	100 ng/mL	2 µl
PBS + 0.1% BSA	100000 ng/mL	200 ng/mL	0.8 µl
10 mM acetic acid + 0.1% BSA	100000 ng/mL	200 ng/mL	0.8 µl
PBS	23000 µM	100 µM	1.74 µl

MMP7 protein concentration in supernatant was measured using the Quantikine Human Total MMP7 Immunoassay ELISA kit - R&D Systems, catalogue number DMP700.

1. Imaging settings - siRNA uptake in A549 cells

Imaging was done on Yokogawa CellVoyager 8000 instrument. The acquisition settings are as follows.
Method: confocal Fluorescence
Objective lens: 20X
Laser wavelengths: 488 nM (green channel), 561 nM (blue channel) and 640 nM (red channel)

1.1 Compounds list

Paraformaldehyde, 4% in PBS, ThermoFisher Scientific, catalogue number J61899-AK
SuperBlock solution, ThermoFisher Scientific, catalogue number 37517
Dako Antibody Diluent, Agilent, catalogue number S3022
Primary antibody: ITGB6 Sheep Polyclonal Antibody, Invitrogen, catalogue number PA5-47588
Secondary antibody: Alexa Fluor 488 labelled antibody, Donkey anti-Sheep IgG, Invitrogen, catalogue number A-11015
Hoechst 33342 nuclear counterstain, Invitrogen, catalogue number H3570
CellMask Deep Red Plasma Membrane stain, Invitrogen, catalogue number C10046
CellMask Green Plasma Membrane stain, Invitrogen, catalogue number C37608
PBS (1X), Gibco, catalogue number 10010023

1.2 Staining protocols

1.2.1 αVβ6 surface staining

Plated cells were cooled on ice. Medium was removed and 100 µl SuperBlock solution was added per well and the plate was incubated in fridge for 1 hour. The SuperBlock solution was removed and 50 µl of 1:50 diluted primary antibody solution was added per well. The plate was incubated in fridge for 1 hour. The primary antibody solution was removed, and the plate was washed with cold 100 µl PBS 2 times per well. 50 µl of 1:500 diluted secondary antibody was added per well and the plate was incubated in fridge for 1 hour. The wells were washed with cold 100 µl PBS 2 times per well. 100 µl of 4% paraformaldehyde (PFA) solution was added per well, and the plate was incubated at room temperature for 20 minutes. The PFA solution was removed, and the plate was then wash 3 times with PBS. 50 µl of 1:5000 diluted Hoechst (in PBS) and 1:1000 diluted CellMask Deep Red (in PBS) were added per well followed by incubation at room temperature for 30 minutes. The wells were washed once with PBS and 100 µl PBS was added. The plate was sealed with black adhesive plate seal and stored in fridge (short term) until imaging.

1.2.2 siRNA uptake

Medium was removed 6h post-treatment with fluorescent labelled naked and SM-conjugated siRNA, and cells were carefully washed three times with PBS. The cells were fixed with 100 µl of 4% PFA for 30 minutes at room temperature. The wells were then washed twice with PBS and 50 µl of 1:5000 diluted Hoechst (in PBS) and 1:100000 diluted CellMask Green (in PBS) were added per well, followed by incubation at room temperature for 30 minutes. The wells were washed once with PBS and 100 µl PBS was added. The plate was sealed with black adhesive plate seal and stored in fridge (short term) until imaging.

2. Imaging settings – siRNA uptake in alveolar organoids

Imaging was done on Yokogawa CellVoyager 8000 instrument. The acquisition settings are as follows. Note that the images were taken at multiple heights within each well, 20 µm in ascending order.
Ascending distance: 800.0 µm
Slicing interval: 20.0 µm
Method: confocal Fluorescence
Objective lens: 20X Long WD (working distance)
Laser wavelengths: 405 nM (blue channel) and 488 nM (red channel)

2.1 Compounds list

Paraformaldehyde, 4% in PBS, ThermoFisher Scientific, catalogue number J61899-AK
Hoechst 33342 nuclear counterstain, Invitrogen, catalogue number H3570
PBS (1X), Gibco, catalogue number 10010023

2.2 siRNA uptake protocol

Fluorescent labelled naked and SM-conjugated siRNA and transfection controls were added to the live organoids. 6h post-treatment, the medium was carefully removed, and the organoids were immediately fixated with 2% paraformaldehyde for 1h at room temperature.
Note: The Matrigel forms a solid gel matrix at approximately 37 °C. However, bellow ambient temperatures the gel begins to break down and liquifies when the temperature reaches approximately 4 °C. Hence, do not cool the plate on ice prior to fixation.
Following the fixation, the PFA solution was removed and the organoids were washed twice with PBS. 50 µl of Hoechst nuclear counter stain was then added to each well, followed by 30 minutes incubation at room temperature. The wells were washed once with PBS and 100 µl PBS was added per well. The plate was sealed with black adhesive plate seal and stored in fridge (short term) until imaging.

RNA extraction protocol

Total RNA isolation and purification from A549 cells were all done using the RNeasy 96 kit from Qiagen (cat. # 74181) according to the manufacturer's recommendation. Protocol for spin technology (centrifugation) was used, see page 35 of RNeasy 96 Handbook. The protocol is summarized below to provide a general overview of the process. All centrifugations were done at 6000 rpm at room temperature.

1. Culture medium was removed and wells containing the cells were washed with PBS. Cells were then lysed by addition of 150 µl Buffer RLT per well (Qiagen, cat. # 79216).
2. Equal volume of 70% ethanol was added to each well and mixed thoroughly.
3. Samples are then added to the RNeasy 96plate and centrifuged for 4 minutes at room. The optional DNase digestion step was skipped.
4. 800 µl Buffer RW1 (included in the kit) and the plate was centrifuged for 4 minutes.
5. 800 µl Buffer RPE was then added to the plate and centrifuged for 4 minutes. This step was repeated with centrifugation done for 10 minutes to dry the columns.
6. The RNeasy 96 plate was then mounted on an elution plate (included in the kit). RNA was eluted with 50 µl of RNase-free water per well.
7. RNA concentration was quantified via NanoDrop.
8. RNA samples were frozen at -80 °C until further use.

Total RNA isolation and purification from human lung alveolar organoids were done using the Direct-zol-96 kit from Zymo Research (catalogue number R2056). The extraction was performed according to the manufacturer's protocol. The protocol is summarized below to provide a general overview of the process. All centrifugations were performed at 6000 rpm for 5 minutes, at room temperature.

1. The culture medium was carefully removed and the organoids were lysed by addition of 150 µl QIAzol Lysis Reagent from QIAGEN (catalogue number 79306), and mixed thoroughly by pipetting up and down to fully dissolve the Matrigel.
2. 150 µl 95-100% ethanol was added to each well and the content was transferred to the Zymo-Spin I-96 Plate, mounted on a Collection Plate.
3. 400 µl RNA Wash Buffer was added to each well and centrifuged.
4. 40 µl of DNase I solution was prepared by mixing 5 µl DNase I and 35 µl DNA Digestion Buffer and added to each well. Wells were centrifuged after 15 minutes of incubation at room temperature.

5. 400 µl Direct-zol RNA PreWash was added to each well and centrifuged. This step was repeated once more.
6. 800 µl RNA Wash Buffer was added per well and centrifuged. Additional centrifugation was done to dry the columns. The plate was then mounted on an Elution Plate.
7. RNA was eluted with 25 µl DNase/RNase-free water
8. RNA concentration was quantified via NanoDrop.
9. RNA samples were frozen at -80 °C until further use.

cDNA synthesis protocol

Isolated RNA samples were reverse transcribed using the High Capacity cDNA Reverse Transcription Kit from Applied Biosystems, Thermo Fisher Scientific (cat. # 4368814 or 4368813). The cDNA synthesis kit is suitable for maximum of 1 µg RNA input. Hence when needed, RNA was diluted with RNase-free water to adjust for this limit. The protocol is done with all components on ice. The steps are summarized below to provide a general overview of the process.

1. A 2X Reverse Transcription master mix was prepared as shown in the table.

cDNA Master Mix Components	Volume per reaction (1X)
10X RT Buffer	2.0 µl
25X dNTP Mix	0.8 µl
10X RT Random Primers	2.0 µl
MultiScribe Reverse Transcriptase	1.0 µl
RNase-free H_2O	4.2 µl
Total per reaction	10.0 µl

2. 10 µl of the master mix and 10 µl of RNA was added to standard profile 96-well non-skirted PCR plate from VWR (cat. # 732-2387)
3. Negative controls were included as
    - No Template Control (NTC) – 10 µl RNase-free water + 10 µl master mix
    - No Reverse Transcriptase Control (NRT) – 10 µl RNA + 10 µl of master mix with MultiScribe Reverse Transcriptase omitted.
4. PCR plate was sealed with adhesive film provided by VWR and spun down for 1 minute at 700-800 x g.
5. Plate is put into a thermocycler (VeritiPro, 96 well from Applied Biosystems, Thermo Fisher Scientific) with the following program.

Settings	Step 1	Step 2	Step 3	Step 4
Temperature	25°C	37°C	85°C	4°C
Time	10 minutes	120 minutes	5 minutes	∞

6. cDNA is stored at 4°C (short-term) or -20 °C (long-term) until further use.

Quantitative polymerase chain reaction protocol

Quantitative polymerase chain reaction (qPCR) is the golden standard technique used for studying gene expression levels. It expands upon the conventional PCR methodology, by utilizing fluorescent reporter molecules to track the accumulation of amplification products in real time. In this thesis, siRNA-induced knockdown, and consequently the difference between relative fold-changes of target expressions were measured using TaqMan probe-based reporter molecules and QuantStudio 7 Flex qPCR systems from Thermo Fisher Scientific. In TaqMan probe-based qPCR assays, the reporter is comprised of a short oligonucleotide sequence complementary to the target sequence. Additionally, the probe contains a complex of quencher and fluorescent reporter dye. During primer extension, the probe binds to the target sequence and the reporter dye is cleaved off by DNA polymerase, freely emitting a fluorescent signal. Target transcript expression levels are therefore determined by how fast the free

reporter dye accumulate and reach a fluorescence signal detection threshold. The faster the signal is detected, the higher the initial target concentration is from the start. The number of amplification cycles required to reach the detection threshold is called a threshold cycle, or Ct-value for short. Analysis of the Ct-values can be done in different ways. In this thesis, fold-change differences in target expression were obtained using the ΔΔCt method. This method requires additional internal control genes to account for biological variations such as cell density and growth differences during the incubation steps, inconsistencies in RNA extraction and cDNA synthesis. The internal controls are housekeeping genes that have similar expression levels across all treatments. Not all housekeeping genes perform equally, thus appropriate controls used in the different in vitro systems here have been previously validated in other studies. For more information on the theory behind qPCR, the reader is referred to the *Introduction to Gene Expression* handbook provided by Thermo Fisher Scientific (Introduction to Gene Expression, Pub. no. 4454239).

All qPCR samples were prepared by adding 7 µl of qPCR reaction master mix and 3 µl of cDNA. The master mix was prepared according to the table below. cDNA samples were diluted prior to mixing with the master mix. The dilutions were based on the cDNA input concentrations, approximate target expression levels and number of target probes used for the specific study. Each study included two endogenous control probes (housekeeping genes) that were used to normalize the Ct values across all conditions accordingly. qPCR reaction master mix and cDNA samples were then transferred to 384-well microplates. For each experimental condition, the Ct value of target and housekeeping genes were measured in QuantStudio 7 Flex provided by Thermo Fisher Scientific.

Component	Volume per reaction (1X)
TaqMan Fast Advanced Master Mix (cat. # 4444557)	5 µl
TaqMan probe	0.5 µl
Nuclease-free H_2O	1.5 µl
Total volume per reaction	**7 µl**

List of TaqMan probes and their catalogue number used in this thesis, ordered from ThermoFisher Scientific, is provided in the table below. All probes are labelled with a FAM dye.

TaqMan probes	Catalogue number
ITGB6	Hs00168458_m1
UBC	Hs0187171556_st1
MMP7	Hs01042796_m1
RPL13A	Hs04194366_g1
PPIB	Hs00168719_m1
VIM	Hs00958111_m1
KRT17	Hs00356958_m1
SPC	Hs00161628_m1
ACTB	Hs01060665_g1
CXCL8	Hs00174103_m1
IL6	Hs00174131_m1
ACTA2	Hs00426835_g1
HPRT1	Hs02800695_m1
SDHA	Hs00188166_m1

Calculations

Condition refers to the treatment done on the cells. Each condition contains three biological replicates. When doing qPCR, there are additional technical replicates for each biological replicate. The number of technical replicates depends on the type of experiment and pipetting instrument used. We opted for two technical replicates per TaqMan probe for all the gene expression studies in this thesis.

Consequently, the Ct values for each TaqMan probe is measured twice per biological replicate. The more TaqMan probes are used for an experiment, the more rows are added to the qPCR plate. If three probes were tested per sample, total of 18 µl cDNA (3 µl cDNA * 3 probes * 2 technical replicates/probe) would be required.

After acquiring the Ct values, the relative fold-change of target expression were calculated as follows. First, the Ct values of technical replicates per biological replicate were averaged for each gene. Since the standard protocol requires two HKG probes to be used as endogenous controls, the two HKG values are again averaged together.

$$Ct_{average}(target) = \frac{Ct\ (technical\ replicate\ 1) + Ct\ (technical\ replicate\ 2)}{2}$$

$$Ct_{average}(HKG) = \frac{Ct_{average}\ (HKG\ 1) + Ct_{average}\ (HKG\ 2)}{2}$$

ΔCt per biological replicate was then calculated by subtracting the corresponding $Ct_{average}$ (HKG) from $Ct_{average}$(target). The subtraction normalizes the Ct value of the target gene to the HKG.

$$\Delta Ct(target) = Ct_{average}\ (target\ ) - Ct_{average}\ (HKG)$$

ΔΔCt is calculated by normalizing the ΔCt values to vehicle control.

$$\Delta\Delta Ct\ (target) = \Delta Ct\ (target\ ) - \Delta Ct\ (vehicle\ control)$$

Relative fold-change of gene expression to vehicle control is calculated by

$$Fold\ change\ to\ vehicle = 2^{-\Delta\Delta Ct\ (target)}$$

Gene expression levels are shown as relative n-fold-changes, normalized to vehicle control (PBS). An expression level of 1 therefore means no change in relative basal expression of the marker compared to vehicle control, while 2 denotes a 2-fold upregulation relative to vehicle control and values lower than 1 denote downregulation of the marker expression as compared to vehicle control.

References

Akhmetshina, A., Palumbo, K., Dees, C., Bergmann, C., Venalis, P., Zerr, P., . . . Distler, J. H. (2012). Activation of canonical Wnt signalling is required for TGF-β-mediated fibrosis. *Nature Communications, 3*, 735. doi:https://doi.org/10.1038/ncomms1734

Almeida, A., Li, Z., Bush, E. W., Pei, T., Glebocka, A., Nicholas, A., Inc, A. P. (2019). *United States of America Patent No. US-20190248832-A1.* Retrieved from https://patents.google.com/patent/US20190248832A1

Arrowhead Pharmaceuticals. (2022, July 5). Retrieved from Arrowhead Pharmaceuticals Initiates Phase 1/2a Studies for Two Pulmonary Candidates ARO-MUC5AC and ARO-RAGE: https://ir.arrowheadpharma.com/news-releases/news-release-details/arrowhead-pharmaceuticals-initiates-phase-12a-studies-two

Arrowhead Pharmaceuticals. (2023, February 2). Retrieved from Arrowhead Pharmaceuticals Initiates Phase 1/2a Study of ARO-MMP7 for Treatment of Idiopathic Pulmonary Fibrosis: https://ir.arrowheadpharma.com/news-releases/news-release-details/arrowhead-pharmaceuticals-initiates-phase-12a-study-aro-mmp7

Bandyopadhyay, A., & Raghavan, S. (2009). Defining the role of integrin αvβ6 in cancer. *Current drug targets, 10*(7), 645–652. doi:https://doi.org/10.2174/138945009788680374

Burgoyne, R. A., Fisher, A. J., & Borthwick, L. A. (2021). The Role of Epithelial Damage in the Pulmonary Immune Response. *Cells, 10*(10), 2763. doi:https://doi.org/10.3390/cells10102763

Chen, H., Tang, J., Liang, J., Huang, D., Pan, C., Liu, S., Tao, L. (2023). Clinical association study on the matrix metalloproteinase expression in the serum of patients with connective tissue disease complicated with interstitial lung disease. *Archives of rheumatology, 38*(3), 367–374. doi:https://doi.org/10.46497/ArchRheumatol.2023.9547

Chen, K. J., Li, Q., Wen, C., Duan, Z. X., Zhang, J., Xu, C., & Wang, J. M. (2016). Bleomycin (BLM) Induces Epithelial-to-Mesenchymal Transition in Cultured A549 Cells via the TGF-β/Smad Signaling Pathway. *Journal of Cancer, 7*(11), 1557-1564. doi:https://doi.org/10.7150/jca.15566

Courtwright, A. M., & El-Chemaly, S. (2019). Telomeres in Interstitial Lung Disease: The Short and the Long of It. *Annals of the American Thoracic Society, 16*(2), 175–181. doi:https://doi.org/10.1513/AnnalsATS.201808-508CME

Craig, V. J., Zhang, L., Hagood, J. S., & Owen, C. A. (2015). Matrix metalloproteinases as therapeutic targets for idiopathic pulmonary fibrosis. *American Journal of Respiratory Cell and Molecular Biology, 53*(5), 585–600. doi:https://doi.org/10.1165/rcmb.2015-0020tr

Crame, E. E., Bowen, J. M., Secombe, K. R., Coller, J. K., François, M., Leifert, W., & Wardill, H. R. (2021). Epithelial-Specific TLR4 knockout challenges Current evidence of TLR4 homeostatic control of gut permeability. *Inflammatory Intestinal Diseases, 6*(4), 199-209. doi:https://doi.org/10.1159/000519200

Decaris, M. L., Schaub, J. R., Chen, C., Cha, J., Lee, G. G., Rexhepaj, M., Turner, S. M. (2021). Dual inhibition of αvβ6 and αvβ1 reduces fibrogenesis in lung tissue explants from patients with IPF. *Respiratory Research, 22*, 265. doi:https://doi.org/10.1186/s12931-021-01863-0

Deng, Z., Fan, T., Xiao, C., Tian, H., Zheng, Y., Li, C., & He, J. (2024). TGF-β signaling in health, disease and therapeutics. *Signal Transduction and Targeted Therapy, 9*, 61. doi:https://doi.org/10.1038/s41392-024-01764-w

Distler, J. H., Györfi, A., Ramanujam, M., Whitfield, M. L., Königshoff, M., & Lafyatis, R. (2019). Shared and distinct mechanisms of fibrosis. *Nature Reviews Rheumatalogy, 15*, 705–730. doi:https://doi.org/10.1038/s41584-019-0322-7

Dowdy, S. F. (2023). Endosomal escape of RNA therapeutics: How do we solve this rate-limiting problem? *RNA Society, 28*(4), 396–401. doi:https://doi.org/10.1261/rna.079507.122

Effendi, W. I., & Nagano, T. (2022). The Hedgehog Signaling Pathway in Idiopathic Pulmonary Fibrosis: Resurrection Time. *International Journal of Molecular Sciences, 23*(1), 171. doi:https://doi.org/10.3390/ijms23010171

Franzén, L., Lindvall, M. O., Hühn, M., Ptasinski, V., Setyo, L., Keith, B. P., Hornberg, J. J. (2024). Mapping spatially resolved transcriptomes in human and mouse pulmonary fibrosis. *Nature Genetics, 56*, 1725–1736. doi:https://doi.org/10.1038/s41588-024-01819-2

Gill, S. E., Nadler, S. T., Li, Q., Frevert, C. W., Park, P. W., Chen, P., & Parks, W. C. (2016). Shedding of Syndecan-1/CXCL1 complexes by matrix metalloproteinase 7 functions as an epithelial checkpoint of neutrophil activation. *American Journal of Respiratory Cell and Molecular Biology, 55*(2), 243–251. doi:https://doi.org/10.1165/rcmb.2015-0193oc

Glass, D. S., Grossfeld, D., Renna, H. A., Agarwala, P., Spiegler, P., DeLeon, J., & Reiss, A. B. (2022). Idiopathic pulmonary fibrosis: Current and future treatment. *The Clinical Respiratory Journal,, 16*(2), 84–96. doi:https://doi.org/10.1111/crj.13466

Han, J., Li, X., Du, J., Xu, F., Wei, Y., Li, H., & Zhang, Y. (2015). Elevated matrix metalloproteinase-7 expression promotes metastasis in human lung carcinoma. *World Journal of Surgical Oncology, 13*, 5. doi:https://doi.org/10.1186/1477-7819-13-5

Henderson, N. C., Rieder, F., & Wynn, T. A. (2020). Fibrosis: from mechanisms to medicines. *Nature, 587*, 555–566. doi:https://doi.org/10.1038/s41586-020-2938-9

Heukels, P., Moor, C., Von Der Thüsen, J. H., Wijsenbeek, M., & Kool, M. (2019). Inflammation and immunity in IPF pathogenesis and treatment. *Respiratory Medicine, 147*, 79-91. doi:https://doi.org/10.1016/j.rmed.2018.12.015

Horan, G. S., Wood, S., Ona, V., Li, D. J., Lukashev, M. E., Weinreb, P. H., Violette, S. M. (2007). Partial Inhibition of Integrin αvβ6 Prevents Pulmonary Fibrosis without Exacerbating Inflammation. *American Journal of Respiratory and Critical Care Medicine, 177*(1), 56–65. doi:https://doi.org/10.1164/rccm.200706-805oc

Huang, Y., Hong, J., Zheng, S., Ding, Y., Guo, S., Zhang, H., Liang, Z. (2011). Elimination pathways of systemically delivered siRNA. *Molecular therapy: the journal of the American Society of Gene Therapy, 19*(2), 381–385. doi:https://doi.org/10.1038/mt.2010.266

Jacob, A., Vedaie, M., Roberts, D. A., Thomas, D. C., Villacorta-Martin, C., Alysandratos, K., Kotton, D. N. (2019). Derivation of self-renewing lung alveolar epithelial type II cells from human pluripotent stem cells. *Nature Protocols, 14*, 3303–3332. doi:https://doi.org/10.1038/s41596-019-0220-0

Jaffar, J., Wong, M., Fishbein, G. A., Alhamdoosh, M., McMillan, L., Gamell-Fulla, C., Westall, G. (2022). Matrix metalloproteinase-7 is increased in lung bases but not apices in idiopathic pulmonary fibrosis. *ERJ open research, 8*(4), 00191. doi:https://doi.org/10.1183/23120541.00191-2022

Kasai, H., Allen, J. T., Mason, R. M., Kamimura, T., & Zhang, Z. (2005). TGF-β1 induces human alveolar epithelial to mesenchymal cell transition (EMT). *Respiratory Research, 6*, 56. doi:https://doi.org/10.1186/1465-9921-6-56

Kozlowski, M. T., Crook, C. J., & Ku, H. T. (2021). Towards organoid culture without Matrigel. *Nature Communications Biology, 4*, 1387. doi:https://doi.org/10.1038/s42003-021-02910-8

Li, D., Zhang, X., Song, Z., Zhao, S., Huang, Y., Qian, W., & Cai, X. (2024). Advances in common in vitro cellular models of pulmonary fibrosis. *Immunology and Cell Biology, 102*, 557-569. doi:https://doi.org/10.1111/imcb.12756

Liu, Y., Chen, W., Zheng, F., Yu, H., & Wei, K. (2022). Xanthatin Alleviates LPS-Induced Inflammatory Response in RAW264.7 Macrophages by Inhibiting NF-κB, MAPK and STATs Activation. *Molecules, 27*(14), 4603. doi:https://doi.org/10.3390/molecules27144603

McGuire, J. K., Li, Q., & Parks, W. C. (2003). Matrilysin (Matrix metalloproteinase-7) mediates E-Cadherin ectodomain shedding in injured lung epithelium. *American Journal of Pathology, 162*(6), 1831–1843. doi:https://doi.org/10.1016/s0002-9440(10)64318-0

Mei, Q., Liu, Z., Zuo, H., Yang, Z., & Qu, J. (2022). Idiopathic Pulmonary Fibrosis: An Update on Pathogenesis. *Frontiers Respiratory Pharmacology, 12*. doi:https://doi.org/10.3389/fphar.2021.797292

Moumné, L., Marie, A.-C., & Crouvezier, N. (2022). Oligonucleotide Therapeutics: From Discovery and Development to Patentability. *Pharmaceutics, 14*(2), 260. doi:https://doi.org/10.3390/pharmaceutics14020260

n.d. (2020, July 1). *Idiopathic pulmonary fibrosis*. Retrieved from MedlinePlus Genetics, National Library of Medicine: https://medlineplus.gov/genetics/condition/idiopathic-pulmonary-fibrosis/

n.d. (2023, January 30). *Study of ARO-MMP7 Inhalation Solution in Healthy Subjects and Patients With Idiopathic Pulmonary Fibrosis*. Retrieved from ClinicalTrials.gov. Identifier: NCT05537025: https://clinicaltrials.gov/study/NCT05537025?cond=IPF&term=arrowhead%20pharmaceuticals&rank=1

n.d. (n.d.). *Introduction to Gene Expression - Getting Started Guide.* Retrieved from Applied Biosystems: https://assets.thermofisher.com/TFS-Assets/LSG/manuals/4454239_IntrotoGeneEx_GSG.pdf

Nighot, M., Al-Sadi, R., Guo, S., Rawat, M., Nighot, P., Watterson, M. D., & MA, T. (2017). Lipopolysaccharide-Induced Increase in Intestinal Epithelial Tight Permeability Is Mediated by Toll-Like Receptor 4/Myeloid Differentiation Primary Response 88 (MyD88) Activation of Myosin Light Chain Kinase Expression. *American Journal of Pathology, 187*(12), 2698-2710. doi:https://doi.org/10.1016/j.ajpath.2017.08.005

Olajuyin, A., Zhang, X., & Ji, H. (2019). Alveolar type 2 progenitor cells for lung injury repair. *Nature Cell Death Discovery, 5*, 63. doi:https://doi.org/10.1038/s41420-019-0147-9

Ou, S. C., Bai, K. J., Cheng, W. H., Chen, J. Y., Lin, C. H., Wen, H. C., & Chen, B. C. (2020). TGF-β Induced CTGF Expression in Human Lung Epithelial Cells through ERK, ADAM17, RSK1, and C/EBPβ Pathways. *International journal of molecular sciences, 21*(23), 9084. doi:https://doi.org/10.3390/ijms21239084

Paranjapye, A., Mutolo, M. J., Ebron, J. S., Leir, S. H., & Harris, A. (2020). The FOXA1 transcriptional network coordinates key functions of primary human airway epithelial cells. *American journal of physiology: Lung cellular and molecular physiology, 319*(1), L126–L136. doi:https://doi.org/10.1152/ajplung.00023.2020

Pardo, A., Cabrera, S., Maldonado, M., & Selman, M. (2016). Role of matrix metalloproteinases in the pathogenesis of idiopathic pulmonary fibrosis. *Respiratory Research, 17*, 23. doi:https://doi.org/10.1186/s12931-016-0343-6

Pardo, A., Gibson, K., Cisneros, J., Richards, T. J., Yang, Y., Becerril, C., Kaminski, N. (2005). Up-Regulation and profibrotic role of osteopontin in human idiopathic pulmonary fibrosis. *PLoS Medicine, 2*(9), 251. doi:https://doi.org/10.1371/journal.pmed.0020251

Ptasinski, V., Monkley, S. J., Öst, K., Tammia, M., Alsafadi, H. N., Overed-Sayer, C., . . . Murray, L. A. (2023). Modeling fibrotic alveolar transitional cells with pluripotent stem cell-derived alveolar organoids. *Life Science Alliance, 6*(8), 202201853. doi:https://doi.org/10.26508/lsa.202201853

Richards, T. J., Park, C., Chen, Y., Gibson, K. F., Di, Y. P., Pardo, A., Zhang, Y. (2012). Allele-specific transactivation of matrix metalloproteinase 7 by FOXA2 and correlation with plasma levels in idiopathic pulmonary fibrosis. *AJP Lung Cellular and Molecular Physiology, 302*, L746–L754. doi:https://doi.org/10.1152/ajplung.00319.2011

Richeldi, L., Collard, H. R., & Jones, M. G. (2017). Idiopathic pulmonary fibrosis. *The Lancet, 389*(10082), 1941-1952. doi:https://doi.org/10.1016/S0140-6736(17)30866-8

Roberts, T. C. (2015). The microRNA Machinery. In G. Santulli, *microRNA: Basic Science* (1st ed., Vol. 887, pp. 15-30). Springer Cham. doi:https://doi.org/10.1007/978-3-319-22380-3_2

Roberts, T. C., Langer, R., & Wood, M. J. (2020). Advances in oligonucleotide drug delivery. *Nature Reviews Drug Discovery, 19*, 673-694. doi:https://doi.org/10.1038/s41573-020-0075-7

Rosas, I. O., Richards, T. J., Konishi, K., Zhang, Y., Gibson, K., Lokshin, A. E., Kaminski, N. (2008). MMP1 and MMP7 as potential peripheral blood biomarkers in idiopathic pulmonary fibrosis. *PLoS Medicine, 5*(4), 93. doi:https://doi.org/10.1371/journal.pmed.0050093

Sacchi, M., Bansal, R., & Rouwkema, J. (2020). Bioengineered 3D models to recapitulate tissue fibrosis. *Trends in Biotechnology, 38*(6), 623-636. doi:https://doi.org/10.1016/j.tibtech.2019.12.010

Saini, G., Porte, J., Weinreb, P. H., Violette, S. M., Wallace, W. A., McKeever, T. M., & Jenkins, G. (2015). αvβ6 integrin may be a potential prognostic biomarker in interstitial lung disease. *European Respiratory Journal, 46*(2), 486–494. doi:https://doi.org/10.1183/09031936.00210414

Sgalla, G., Iovene, B., Calvello, M., Ori, M., Varone, F., & Richeldi, L. (2018). Idiopathic pulmonary fibrosis: pathogenesis and management. *Respiratory Research, 19*, 32. doi:https://doi.org/10.1186/s12931-018-0730-2

Slack, R. J., Macdonald, S., Roper, J., Jenkins, R., & Hatley, R. (2022). Emerging therapeutic opportunities for integrin inhibitors. *Nature Reviews Drug Discovery, 21*, 60–78. doi:https://doi.org/10.1038/s41573-021-00284-4

Sun, L., Xing, J., Zhou, X., Song, X., & Gao, S. (2024). Wnt/β-catenin signalling, epithelial-mesenchymal transition and crosslink signalling in colorectal cancer cells. *Biomedicine & Pharmacotherapy, 175*, 116685. doi:https://doi.org/10.1016/j.biopha.2024.116685

Swanson, L., Katkar, G. D., Tam, J., Pranadinata, R. F., Chareddy, Y., Coates, J., Ghosh, P. (2020). TLR4 signaling and macrophage inflammatory responses are dampened by GIV/Girdin. *Proceedings of the National Academy of Sciences, 117*(43), 26895-26906. doi:https://doi.org/10.1073/pnas.2011667117

Swee, M., Wilson, C. L., Wang, Y., McGuire, J. K., & Parks, W. C. (2008). Matrix metalloproteinase-7 (matrilysin) controls neutrophil egress by generating chemokine gradients. *Journal of Leukocyte Biology, 83*(6), 1404–1412. doi:https://doi.org/10.1189/jlb.0108016

Tirino, V., Camerlingo, R., Bifulco, K., Irollo, E., Montella, R., Paino, F., Pirozzi, G. (2013). TGF-β1 exposure induces epithelial to mesenchymal transition both in CSCs and non-CSCs of the A549 cell line, leading to an increase of migration ability in the CD133+ A549 cell fraction. *Nature Cell Death and Disease, 4*, 620. doi:https://doi.org/10.1038/cddis.2013.144

Wan, H., Dingle, S., Xu, Y., Besnard, V., Kaestner, K. H., Ang, S., Whitsett, J. A. (2005). Compensatory Roles of Foxa1 and Foxa2 during Lung Morphogenesis. *Journal of Biological Chemistry, 280*(14), 13809–13816. doi:https://doi.org/10.1074/jbc.m414122200

White, E. S., Xia, M., Murray, S., Dyal, R., Flaherty, C. M., Flaherty, K. R., Martinez, F. J. (2016). Plasma Surfactant Protein-D, Matrix Metalloproteinase-7, and Osteopontin Index Distinguishes Idiopathic Pulmonary Fibrosis from Other Idiopathic Interstitial Pneumonias. *American Journal of Respiratory and Critical Care Medicine, 194*(10), 1242–1251. doi:https://doi.org/10.1164/rccm.201505-0862oc

Yamaguchi, M., Hirai, S., Tanaka, Y., Sumi, T., Miyajima, M., Mishina, T., Sakuma, Y. (2016). Fibroblastic foci, covered with alveolar epithelia exhibiting epithelial–mesenchymal transition, destroy alveolar septa by disrupting blood flow in idiopathic pulmonary fibrosis. *Laboratory Investigation, 97*(3), 232–242. doi:https://doi.org/10.1038/labinvest.2016.135

Zhang, Y., & Wang, J. (2023). Cellular and Molecular Mechanisms in Idiopathic Pulmonary Fibrosis. *Advances in Respiratory Medicine, 91*(1), 26-48. doi:https://doi.org/10.3390/arm91010005

Zhang, Y., Handley, D., Kaplan, T., Yu, H., Bais, A. S., Richards, T., Kaminski, N. (2011). High throughput determination of TGFB1/SMAD3 targets in A549 lung epithelial cells. *PLoS ONE, 6*(5), 20319. doi:https://doi.org/10.1371/journal.pone.0020319

Zhao, M., Wang, L., Wang, M., Zhou, S., Lu, Y., Cui, H., Yao, Y. (2022). Targeting fibrosis: mechanisms and clinical trials. *Nature Signal Trandsduction and Targeted Therapy, 7*, 206. doi:https://doi.org/10.1038/s41392-022-01070-3

Zhou, B., Liu, H., Xu, F., & Jia, X. (2024). The role of macrophage polarization and cellular crosstalk in the pulmonary fibrotic microenvironment: a review. *Cell Communication and Signaling, 22*, 172. doi:https://doi.org/10.1186/s12964-024-01557-2

Zhou, Y., Ling, T., & Shi, W. (2024). Current state of signaling pathways associated with the pathogenesis of idiopathic pulmonary fibrosis. *Respiratory Research, 25*, 245. doi:https://doi.org/10.1186/s12931-024-02878-z

Zuo, F., Kaminski, N., Eugui, E., Allard, J., Yakhini, Z., Ben-Dor, A., Heller, R. A. (2002). Gene expression analysis reveals matrilysin as a key regulator of pulmonary fibrosis in mice and humans. *Proceedings of the National Academy of Sciences, 99*(9), 6292–6297. doi:https://doi.org/10.1073/pnas.092134099